





UNIVERSITY OF HAMBURG

MASTER'S THESIS

---

# A Global Analysis of Mesoscale Eddy Dynamics via a Surface-Signature-Based Tracking Algorithm

---

*Author:*

NIKOLAUS KOOPMANN

*Co-Supervisor:*

PROF. DR. JOHANNA  
BAEHR

*Supervisor:*

PROF. DR. CARSTEN EDEN

2015/04/28

## Abstract

Several global mesoscale ocean-eddy-dynamics censuses were obtained via an automated, sea-surface-anomaly-based detection- and tracking-algorithm. 12 years of input sea-surface-height data were taken from a satellite-altimetry product and from a global eddy-resolving ocean model. Variables of particular interest were horizontal eddy scale and zonal eddy drift speeds. Motivation was to answer the question whether time- and space-resolutions of the altimeter-product are sufficiently fine to resolve eddy scales accurately and to allow a successful tracking of individual eddies over time. The results suggest that the  $0.25^\circ$ -resolution of the merged satellite scans is insufficient to resolve realistic eddy scales in high latitudes and that a 7 day time-step, albeit generally sufficient to determine zonal eddy drift-speeds, leads to unreliable trackings in regions of very strong drift-vector gradients. The finer resolution in space and time of the model data allows for more robust determinations of eddy scales which turn out to be significantly smaller than those derived from satellite data. Zonal drift speeds are shown to be systematically slower in the model than in the satellite product.

# *Contents*

<b>1</b>	<b>Introduction</b>	<b>5</b>
1.1	Motivation . . . . .	5
1.2	Overview . . . . .	7
<b>2</b>	<b>Methods and Theory</b>	<b>9</b>
2.1	Detection Methods . . . . .	9
2.2	Eddy Drift Speeds . . . . .	12
2.3	Horizontal Eddy Scales . . . . .	14
2.4	Satellite- vs Model-Data . . . . .	15
<b>3</b>	<b>History</b>	<b>19</b>
<b>4</b>	<b>The Algorithm</b>	<b>23</b>
4.1	Data Preparation . . . . .	24
4.2	Rossby Radii and Phase Speeds . . . . .	24
4.3	Finding the Contours . . . . .	25
4.4	Filtering the Contours . . . . .	26
4.5	Tracking . . . . .	34
4.6	Running the Code . . . . .	37
<b>5</b>	<b>Results</b>	<b>39</b>
5.1	MI - 7 day time-step - Aviso . . . . .	41
5.2	MII - 7 day time-step - Aviso . . . . .	44
5.3	MII - 7 day time-step - POP . . . . .	45
<b>6</b>	<b>Discussion</b>	<b>49</b>
6.1	Lengths of Tracks . . . . .	49
6.2	Scales and the Effect of Down-Sampling . . . . .	51
6.3	Drift Speeds . . . . .	52
6.4	MII - 2 day time-step - POP . . . . .	54
6.5	Net Drift Speeds . . . . .	54
<b>7</b>	<b>Summary and Conclusion</b>	<b>57</b>
<b>Appendix A Ideas for the Future</b>		<b>59</b>
<b>Appendix B 2-Dimensional Turbulence</b>		<b>63</b>
<b>Appendix C Eddy Categories</b>		<b>67</b>

<b>Appendix D Derivations</b>	<b>69</b>
<b>Appendix E Legend</b>	<b>73</b>
<b>Bibliography</b>	<b>77</b>

# 1

## Introduction

THE MAIN PURPOSE of this study is to investigate the dynamics of mesoscale ocean eddies on a global scale, *i.e.* to provide a statistical census on horizontal scale, lifetime and zonal drift speeds. By virtue of the geostrophic character of the scales of concern, such vortices implicate a local upheaval/depression of density surfaces, usually also including the sea surface<sup>1</sup>.

The resultant *hills* and *valleys* in surface anomaly can be resolved by combining multiple satellite-altimetry signals (see fig. 1.1). One motivation of this study is to investigate whether the resolutions in space and time of such altimeter-derived products suffice to successfully track individual

eddies over long periods of time and to precisely determine their horizontal extent and drift speed. The detection/tracking/analyzing procedure of individual eddies is done globally via an automated parallelized computer-program. To analyze the effects of different time/space-resolutions, a finer-grid SSH-product of a modern ocean-circulation model is subjected to the algorithm as well.

### 1.1 Motivation

GEOSTROPHIC turbulence is typically characterized by rather stable, often deep reaching, more or less circular, coherent pressure anomalies that rotate fluid around in a vortex in quasi-geostrophic equilibrium (Zhang *et al.*, 2013). These entities

<sup>1</sup> As in theory, baroclinic eddies have most of their energy in the first (surface-intensified) baroclinic mode (Olbers *et al.*, 2012).

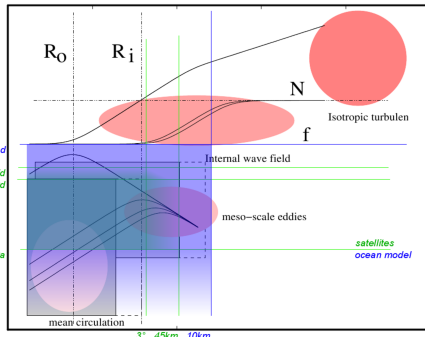


Figure 1.1: Resolutions for model vs satellite.  
Modified version from Olbers *et al.* (2012).

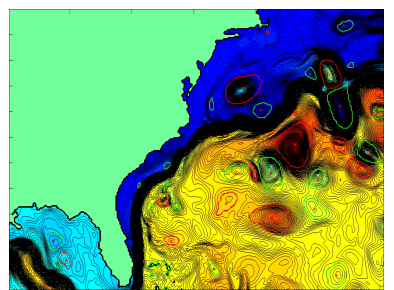


Figure 1.2: Animation snapshot of early test run. Shown is SSH with detected eddies indicated by red and green lines.

can persist for long periods of time in which they often travel distances on the order of hundreds of kilometers zonally. The fact that baroclinic instability leads to these vortices, instead of cascading to ever smaller scales as would be expected from chaotic turbulence, is a direct consequence of the inverse energy cascade of two-dimensional motion<sup>2</sup> (see fig. B.1.) (Charney, 1971; Brachet, 1988). The atmospheric analog are storms and high-pressure systems, yet with much less difference between high- and low-pressure systems in the ocean due to a smaller centrifugal force *i.e.* smaller Rossby number (Ro). These quasi-geostrophic, mesoscale vortices *i.e.* *eddies*<sup>3</sup>, are readily visible on SSH-maps (see fig. 2.2). Yet, it is difficult to *define* an eddy in terms of physical variables. The transition from meandering jet or other undeveloped baroclinic turbulence to a coherent vortex is not very sharp. Eddies also sometimes merge or split or collectively form rifts and valleys in SSH. Detecting them on one snapshot automatically via an algorithm is therefore not trivial. Further complications arise when the algorithm is also supposed to track each individual eddy over time. Their sheer abundance at any given point in time inevitably creates ambiguities as to *which is which* between time steps.

FROM the automated-tracking censuses that have thus far been presented (Chelton *et al.* (2011, 2007); Petersen *et al.* (2013)) and from the numerous publications of investigations into geostrophic scales and phase speeds via satellite SSH products by other means (*e.g.* spectral methods, (Scott & Wang, 2005; Chelton *et al.* , 2011; Stammer, 1997)) it appears that results critically depend on the resolution of the particular SSH product used and/or the methods by which said parameters were derived, as scales, phase speeds and other parameters generally do not agree very well among the different publications. Comparison to theory is usually also rather unsatisfactory which should come as no surprise since the physics of non-linear eddies are still far from complete so that results can usually only be compared to linear theory.

THE main questions that motivated this work therefor are:

1. How should an eddy be *defined* and how should this understanding be implemented in the algorithm? Do the different approaches affect the results?
2. Is it possible to derive realistic horizontal eddy scales from satellite altimetry products via an automated SSH-based eddy-census. How should such scale be defined and is the resolution in time and space of the Aviso product sufficient for precise determinations? What are those scales?
3. Is it possible to automatically track eddies and use those

<sup>2</sup> For a discussion of this phenomenon see appendix B.

<sup>3</sup> For a discussion of the different types of vortices in the ocean see appendix C.

tracks to derive eddy drift vectors? How reliable is the tracking and to what extent is its quality influenced by resolution in time? How do the zonal drift speeds compare to theory?

4. How do scales and drift speeds derived from satellite [SSH](#) compare to those derived from eddy-resolving ocean model [SSH](#)?

## 1.2 Overview

DUE to the inherently technical character of the matter, large parts of this text are dedicated to details of the algorithm (see chapter 4). Oceanographic results are treated in the [Results](#)- and [Discussion](#)-chapters. The [Methods and Theory](#) chapter outlines the different approaches to detect eddies from [SSH](#), explains the mechanism of the [westward drift](#) of eddies, discusses the [horizontal scale](#) of eddies and explains its relevance to climate models and shows the [differences](#) of the two data sets (satellite vs model). The [History](#) chapter introduces a handful of relevant historical papers. Results of the different censuses are presented in the [Results](#) chapter and discussed in the [Discussion](#). The quintessence of the findings is summarized in the [Conclusions](#)-chapter. Several further, thus far incomplete, topics are touched in the [Ideas for the Future](#)-appendix. The theoretical [Eddy](#)- and [Turbulence](#)-appendices and the [Derivations](#)-appendix reflect preliminary theoretical thoughts of the author and are meant as a bonus.



## 2

# *Methods and Theory*

### 2.1 Detection Methods

- One way to find an eddy in **SSH** is to simply scan for closed contours at different vertical levels and then subject each found ring to a series of geometrical tests to decide whether that contour qualifies. Only if all criteria are met is an eddy found. This method was first used by [Chelton et al. \(2011\)](#) and is a relatively simple yet very effective method. Therefore, as a starting point, this method will be adopted and should also serve as a general definition of what will be referred to as an *eddy* hereafter.

[Chelton et al.](#) set the following threshold criteria for their algorithm:

1. The **SSH** values of all of the pixels are above (below) a given **SSH** threshold for anticyclonic (cyclonic) eddies.
  2. There are at least  $[threshold]$  pixels and fewer than  $[threshold]$  pixels comprising the connected region.
  3. There is at least one local maximum (minimum) of **SSH** for anticyclonic (cyclonic) eddies.
  4. The amplitude of the eddy is at least  $[threshold]$ .
  5. The distance between any pair of points within the connected region must be less than  $[threshold]$ .
- Another frequently used method to define an eddy makes use of the 2d deformation tensor  $\nabla \mathbf{u}$ .

$$\det(\lambda \mathbf{I} - \nabla \mathbf{u}) = 0 \quad (2.1)$$

The sign of its squared eigenvalues indicates whether the flow-field has parabolic, vorticity dominated character, or whether deformation dominates, giving hyperbolic character. Expanding equation (2.1) yields

$$\lambda^2 - \lambda(v_y + u_x) + u_x v_y - u_y v_x = 0 \quad (2.2)$$

Assuming horizontal velocities to be much larger than vertical *i.e.* applying the small aspect-ratio assumption ([Olbers et al., 2012](#)), the motion becomes 2-dimensional and the continuity equation reduces to  $u_x = -v_y$ . Hence

$$\lambda^2 = \mathbf{O}_w / 4 = u_x^2 + u_y v_x \quad (2.3)$$

This is called the Okubo-Weiss-Parameter<sup>1</sup>  $\mathbf{O}_w$  ([Okubo, 1970](#)). Its meaning is further elucidated by interpreting equation (2.3) as<sup>2</sup>:

$$\begin{aligned} \mathbf{O}_w &= s_n^2 + s_s^2 - \omega^2 + \nabla \cdot \mathbf{u} \\ &= (u_x - v_y)^2 + (v_x + u_y)^2 - (v_x - u_y)^2 + (u_x + v_y)^2 \\ &= 4u_x^2 + 4v_x u_y \end{aligned} \quad (2.4)$$

<sup>1</sup> see also derivation 5.

<sup>2</sup> see derivation 4.

where  $s_{n/s}$  are the normal respective shear components of strain. Its sign thus describes the field's tendency for either vorticity- or shear-dominated motion ([Isern-Fontanet, 2006](#)). An area of large negative values of  $\mathbf{O}_w$  indicates high enstrophy density compared to gradients of kinetic energy ([Weiss, 1991](#)), thus indicating little friction paired with high momentum *i.e.* a vorticity-dominated field as would be found in a coherent, angular-momentum-conserving entity. Positive values on the other hand indicate motion dominated by deformation as *e.g.* in-between two vortices of opposite sign. The fourth term, which is irrelevant here, represents divergence and can here be interpreted as negative *vortex stretching* (*e.g.* bathtub sink).

As useful as this parameter seems, it turns out that using it to identify eddies is often not practical. [Chelton et al. \(2011\)](#) name 3 major drawbacks:

- *No single threshold value for  $\mathbf{O}_w$  is optimal for the entire World Ocean. Setting the threshold too high can result in failure to identify small eddies, while a threshold that is too low can lead to a definition of eddies with unrealistically large areas that may encompass multiple vortices, sometimes with opposite polarities.*
- *$\mathbf{O}_w$  is highly susceptible to noise in the SSH field. Especially when velocities are calculated from geostrophy, the sea surface has effectively been differentiated twice and then squared, exacerbating small discontinuities in the data.*
- *The third problem with the W-based method is that the interiors of eddies defined by closed contours of W do not generally coincide with closed contours of SSH. The misregistration of the two fields is often quite substantial.*

In summary, the  $O_w$ -method critically hinges on the necessary assumption of a smooth, purely geostrophic SSH topography and is therefore inferior to the approach of scanning for closed SSH-contours directly (as was done so by Chelton *et al.* (2013)) (see also Zhang *et al.* (2013)).

## 2.2 Eddy Drift Speeds

INTUITIVELY any translative motion of a vortex should stem from an asymmetry of forces as in an imperfectly balanced gyroscope wobbling about and translating across a table. The main effects that cause a quasi-geostrophic ocean eddy to translate laterally can be explained rel. easy heuristically:

### Drift Speed 2.2.1: Lateral Density Gradient

Consider a mean layer-thickness gradient  $\frac{\partial h}{\partial x} > 0$  somewhere in the high northern latitudes and a geostrophic, positive density anomaly within that layer. In other words, a high-pressure vortex or an anti-cyclonic eddy with length scale  $L \approx L_R$ . Next consider a parcel of water adjacent to the eddy's northern flank of initially zero relative vorticity that is being entrained by the eddy. As the clockwise rotating eddy advects the parcel towards its eastern side, the water-column comprising said fluid will be stretched vertically as it is advected towards larger depths. In order to maintain total vorticity a small new relative-vorticity term is introduced via term  $C$  in equation (C.1c). Since the vorticity budget is dominated by the planetary component, this new term has sign of  $f$  i.e. **positive**. The opposite effect holds for a parcel advected towards the western side. Then, vortex *squeezing* leads to a new **negative** relative-vorticity term. Hence water masses on both sides of the thickness gradient acquire rotation that slowly pushes the eddy in the direction  $-f \times \frac{\partial h}{\partial x}$  (in this case south). Note that since vorticity is dominated by the planetary component, the rotational sense of the eddy is irrelevant here. I.e. water columns stretched [squeezed], will always lead to new  $\omega$  with sign of  $f$  [ $-f$ ].

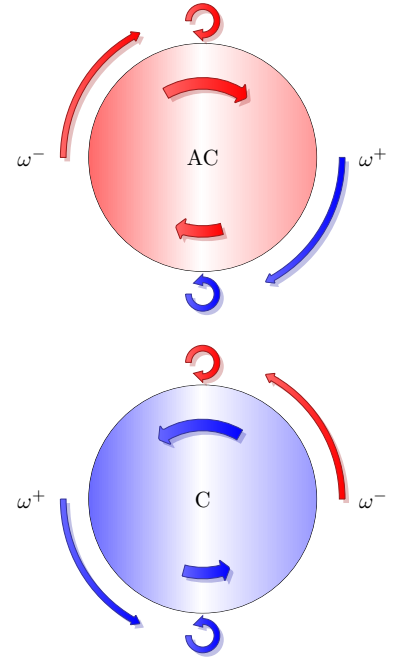


Figure 2.1: Bottom [Top]: Northern hemisphere [anti]cyclone. Blue [red] color indicates presence/production of positive [negative] relative vorticity. Advection of adjacent water masses leads to a westward drift, irrespective of the eddy's sign (see drift-speed-box 2.2.2). Inside, the discrepancy in swirl strength between north and south requires another (smaller) zonal drift term, which is eastward [westward] for [anti]cyclones.

### Drift Speed 2.2.2: Planetary Lift

Assume now that  $\beta L$  be comparable to  $f$  from the previous example. Then, independent of layer-thickness, all fluid adjacent to the eddy on its western and eastern flanks will be transported meridionally, thereby be tilted with respect to  $\Omega$  and hence acquire relative vorticity to compensate. All fluid transported north [south] will balance the increase in planetary vorticity with a decrease [increase] in relative vorticity. This is again independent of the eddy's sense and in this case also independent of hemisphere since  $\frac{\partial f}{\partial y} = \beta > 0$  for all latitudes. The result is that small negative vortices to the northern and small positive vortices

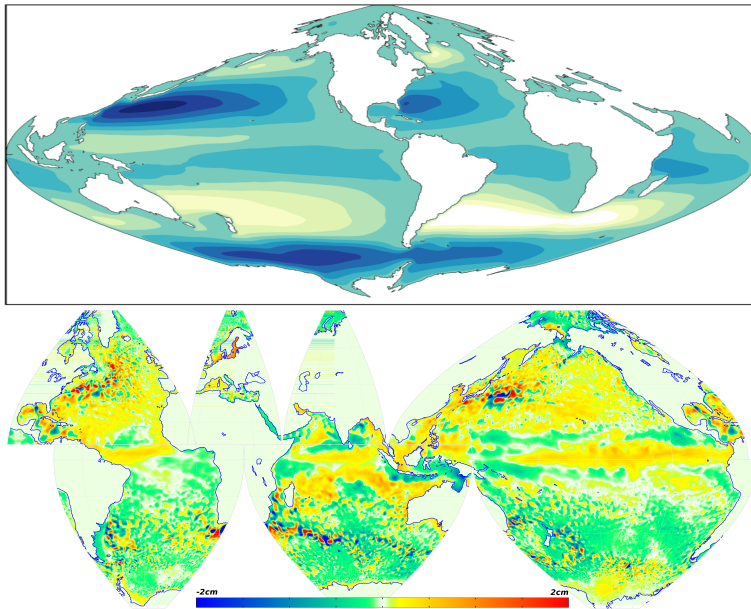


Figure 2.2: Top: Stream function of Stommel's equation  $F_{bottom} - F_{surface} = -V\beta$  with constant eddy viscosity (taken from Author's Bachelor thesis). Bottom: SSH of POP eddy-resolving model snapshot with mean of one year subtracted. Geostrophic turbulence in the form of mesoscale eddies is not resolved by climate models and needs thus to be parameterized. Large-scale dynamics are in part just an integral manifestation of the dynamics on the scales below. Hence, the better the understanding of the mechanisms on the meso-scale, the better they can be parameterized.

to the southern flank of eddies will push them west. This effect is directly analogous to the *conveyer-belt*-like westward creeping of Rossby waves. Theory shows that at first approximation it is indeed equivalent (see e.g. chapter 3).

### Drift Speed 2.2.3: Eddy-Internal $\beta$ -Effect

In the later case clearly particles within the vortex undergo a change in planetary vorticity as well. Or from a different point of view, since orbital speed  $u_o$  is proportional to  $-\nabla p/f$ , particles drifting poleward [equatorward] will be subjected to an increase [decrease] in coriolis force irrespective of eddy sense. Yet, due to conservation of mass,  $u_o$  cannot increase [decrease] when moving poleward [equatorward]. The center of volume must hence be shifted west for an anti-cyclone and east for a cyclone. Or the other way around: The only way to compensate for the discrepancy in Coriolis acceleration north and south, whilst maintaining constant eddy-relative particle speed, is to superimpose a zonal drift velocity so that net particle velocities achieve symmetric Coriolis acceleration. Or yet from another perspective: As particles within a Northern-hemisphere anti-cyclone move north on its western side, they are subjected to an increase in Coriolis force, no longer entirely balanced by the pressure gradient. Hence there will be a tendency for water to *climb up* the thickness gradient, effectively drawing water from outside into the eddy thereby creating a negative pressure anomaly to

the western side of the eddy. Water flowing south on the eastern side undergoes a decrease in Coriolis force, thereby creating a relaxation of the pressure gradient. In other words, the eddy effectively *pulls* itself west on its western side and *pushes* itself west on its eastern side. In the case of a NH-cyclone the increase in  $f$  as water flows north on its eastern side, pushes the negative density anomaly east and water on its western side, relaxing the (negative in  $x$ -direction) pressure gradient, pulls in the thicker layer to the west, thereby pushing the cyclone east. Note that the later example has the same outcome on the Southern hemisphere since there both  $f$  and cyclone/anti-cyclone flip sign.

### 2.3 Horizontal Eddy Scales

THIS section discusses the motivation for exact determinations of eddy scales. That is, their horizontal extent *i.e.* their diameter or *wavelength*.

JUST like the eddy itself, its scale is rather vague and difficult to define. What physical parameter defines the outer edge of a seamless, smooth vortex? If the eddy is detected as done by Chelton *et al.* (2011), *i.e.* closed contours of SSH, the interior of which fulfilling certain criteria, the measured perimeter may jump considerably from one time step to the next. An incremental difference in the choice of  $z$  might translate to a perimeter outlining twice the difference in area, especially when SSH gradients are small. Another possibility is to define an amplitude first, then assume a certain shape *e.g.* Gaussian, and then infer the radius indirectly. The obvious problem with this approach would be to properly define the amplitude. The most physically sound method would have to be one depending on the eddy's most defining physical variable that is unambiguously determinable from SSH: the geostrophic velocities. Chelton *et al.* (2011) tried all methods but conclude that the later is the most adequate one<sup>3</sup>.

<sup>3</sup> See contour-filter 10.

CONSTRUED as an integral length scale of turbulence *i.e.* as the distance at which the auto-correlation of particles reaches zero (Batchelor, 1969; Eden, 2007a), the eddy-scale turns out to be of fundamental relevance for attempts to parameterize geostrophic turbulence. General circulation models ( $\mathcal{O}(10^2)$  km) as they are used in *e.g.* climate forecasts are too coarse to resolve mesoscale ( $\mathcal{O}(10^1)$  km) turbulence (Eden *et al.*, 2007; Eden, 2007a,b; Treguier, 1997; Ferrari & Nikurashin,

2010). Even if the Von-Neumann-condition was ignored and a refinement was desired horizontally only, a leap of one order of magnitude would effect an increase in calculation time<sup>4</sup> of factor  $x = 100$ . The effects of the nonlinear terms therefore have to be somehow articulated in an integral sense for the large grid-boxes in the model (Fox-Kemper *et al.*, 2008; Marshall, 1981; Gent *et al.*, 1995; Killworth, 1998; Gaspar *et al.*, 1990; Griffies, 2004; Bryan *et al.*, 1999). A common approach is to assume that eddy kinetic energy  $\overline{u'u'}$  and eddy potential energy  $\overline{w'p'}$ , akin to diffusive processes<sup>5</sup>, were proportional to the gradient of  $\bar{u}$  respective  $\bar{b}$  (down-gradient-parameterization<sup>6</sup>) (Olbers *et al.*, 2012; Marshall & Adcroft, 2010; Eden, 2012), which leads to the problem of finding expressions for the *turbulent diffusivities* *i.e.* the rate at which gradients are diffused by turbulence. This parameter is by no means constant, instead it can span several orders of magnitude, itself depending on the strength of turbulence-relevant gradients, and sometimes even assuming negative values (Eden & Greatbatch, 2008). Precise knowledge of the integral length scale and the physics that set it is hence vital for attempts to analyze and set values for eddy diffusivities and turbulence parameterizations in general.

#### 2.4 Satellite- vs Model-Data

THE latest **Aviso SSH** product features impressive accuracy, constancy and resolutions in both space and time. This is achieved by collecting all of the data from all of the altimeter-equipped satellites available at any given moment for any given coordinate. This conglomerate of highly inhomogeneous data is then subjected to state-of-the-art interpolation methods to produce a spatially and temporally coherent product. One satellite alone is not sufficient to adequately resolve mesoscale variability globally.

E.g. the Topex/Poseidon satellite had a ground repeat track orbit of 10 days and circled the earth in 112 minutes or  $\approx 13$  times a day with a swath width of 5 km. Hence it drew  $\sim 26$  5-km-wide stripes onto the globe every day. The orbit's precession is such that this pattern is then repeated after 10 days, which means that at the equator only  $10 \times 26 \times 5 = 1300$  km of the  $2\pi \times 6371 = 40\,000$  km get covered, *i.e.* 3.25%. At every 10 day time-step, on average, effectively  $(40000 - 1300)/26 = 1490$  km are left blank in-between swaths on the equator. This is why, no matter how fine the resolution within the swath at one moment in time may be, the spatial resolution is so coarse. The merged ERS-1/Topex-data as used by Chelton *et al.* (2011) has a time step of 7 days. Assuming eddy drift speeds of  $u_e = \mathcal{O}(10^{-1})$  m/s implies a distance traveled per

<sup>4</sup> With the Moore's-Law-type exponential growth in FLOP/S of the last 22 years for supercomputers ( $\lg(x) \sim 3/11a$ ) a factor 100 interestingly translates to only  $a = 22/3 \approx 7$  years ...

<sup>5</sup> In analogy to Fick's first law of diffusion.

<sup>6</sup> *i.e.* Reynolds averaging.

	POP	merged T/P - ERS-1
dx	0.1°	0.25°
dt	1d	7d
$\log_{10} 2$ filter cutoff	–	2° by 2°
z-levels	42	1
variables	SSH, S, T, u/v/w, tracers etc	SSH
pot. interpo- lation artifacts	–	yes
reality	no	yes

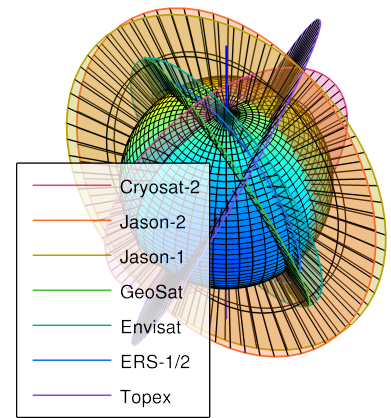


Figure 2.3: Orbit examples.

time step of  $L_{\delta t} \approx 60$  km. Chelton *et al.* estimate their effective spatial resolution as  $\delta x \approx 40$  km. Eddies of smaller scale are not resolved.

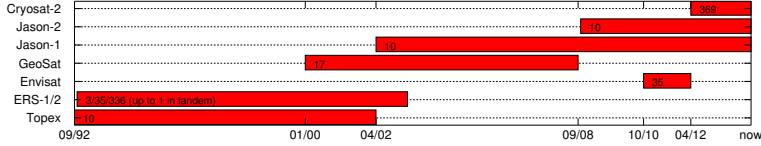


Figure 2.4: Length of mission. Numbers are orbit-period in days. Numbers taken from respective official web pages.

TRACKING a single eddy from one time-step to the next is complicated by the sheer abundance of eddies at any given point in time and the fact that eddy activity is usually concentrated into regions of strong geostrophic turbulence. The ambiguities in matching the eddies from the old time-step to those of the new one might cause aliasing effects in the final statistics. The drift speeds ( $\mathcal{O}(10^1)$  km/day) of eddies are not really the problem here, as they usually translate slow enough to not cover more than 1 grid node per 7 day time step. The issue are those areas where eddies are born, die and merge. According to Smith & Marshall (2009), instabilities within the ACC grow at rates of up to  $1/(2\text{days})$ , which means that at one time-step up to 3 eddies have emerged and equally many died for every eddy identified within such region. The ground-repeat-frequency of a satellite can of course not be set arbitrarily. Especially when the satellite is desired to cover as far north and south as possible, whilst still being subjected to just the right torque from the earth's variable gravitational field to precess at preferably a sun-synchronous frequency *i.e.*  $360^\circ/\text{year}$  (Goldreich, 1965). Neither can the satellite's altitude be chosen arbitrarily. If too low, the oblateness of the earth creates too much eccentricity in the orbit that can no longer be frozen<sup>7</sup>. Another problem could be potential inhomogeneity in the merged data in time dimension, since data of old and current missions are lumped together into one product. This is why Chelton *et al.* (2011) opted against the finest resolution available and instead went for a product that had the most satellites merged in unison for the longest period of time.

<sup>7</sup> Minimizing undulating signals in altitude by choosing the right initial values (Goldreich, 1965).

### Box 1: Horizontal Resolution

Assume  $Bu = 1$ , so that  $L = NH/f$  and  $NH = a/10d$  (corresponds to  $L(\phi = 30^\circ) = 100\text{km}$ ), a model resolution of  $1^\circ/\mu$  and that the eddy diameter is twice the Rossby radius. Then, how many grid notes  $n$  fit into one eddy as a function of latitude?

$$\begin{aligned} n\delta x &= L \\ n \cos \phi \frac{\pi}{180} a &= \frac{2NH}{f} \\ n &= \frac{NH\mu\Omega}{\sin 2\phi} \frac{180}{\pi^2 a} \end{aligned} \quad (2.5)$$

In this flat-bottom, constant  $\rho_z$ , Mercator-gridded model the worst eddy-resolution is interestingly at mid-latitude (see fig. 2.5).

THE finer resolution of the POP data in space and time should certainly yield more precise results. It must be kept in mind though that by using the model data, what one analyses is of course just that - a *model*. Baroclinic geostrophic space/time scales depend crucially on e.g. the vertical density structure (see chapter 3, Charney (1971)), which is resolved only poorly in the model. A useful comparison among satellite/model results should hence be tricky.

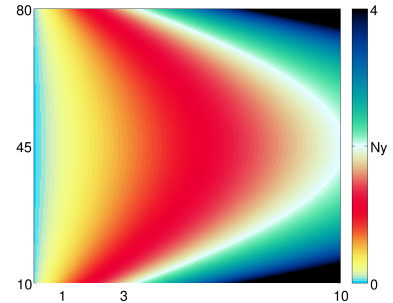


Figure 2.5:  $n(\phi, \mu)$ .  $Ny \equiv 2$  i.e. the Nyquist frequency. See box 1.



### 3

## *Important Papers*

THE following discusses a handful of selected historical papers that are concerned with either the theory of mesoscale eddies or with the detection/tracking of eddies from [SSH](#) data.

### *Waves and Turbulence on a $\beta$ -Plane ([Rhines, 1974](#))*

Rhines investigated the effect of the  $\beta$ -plane on the inverse energy cascade of quasi-2-dimensional atmospheric and oceanic turbulence. At constant  $f$ , energy should be cascaded to ever-larger scales until halted by the scale of the domain. This is clearly not the case, as no storm has ever grown to global scale. The presence of a meridional restoring force creates a critical scale beyond which the *turbulent migration of the dominant scale nearly ceases* .... Rossby waves are excited which would in theory eventually give way to alternating zonal jets of width  $\frac{U}{\beta}$ . This scale was later coined the Rhines Scale  $L_\beta$ .

### *Westward Motion of Mesoscale Eddies ([Cushman-Roisin et al., 1990](#))*

Bjerknes & Holmboe (1944) already noted that the  $\beta$ -effect causes a mass-imbalance in planetary vortices that, if not met by an asymmetry in shape must lead to westward propagation. Nof (1981) derived that the  $\beta$ -effect results in a net meridional force on the integrated mass of the vortex, which in balance with the Coriolis acceleration shoves cyclones eastward and anti-cyclones westward. They also explained how displaced water outside the eddy's perimeter causes a much stronger westward component, with the result that all eddies propagate westward irrespective of rotational sense. The westward drift was also derived in various forms by e.g. Flierl (1984); Matsuura & Yamagata (1982); van Leeuwen (2007).

THE paper by Cushman-Roisin *et al.* (1990) is particularly helpful to understand where the two components of westward

drift come from. By scaling the terms in the one-layer primitive equations by their respective dimensionless numbers, integrating the interface-displacement caused by the eddy over the eddy's domain and applying mass continuity they derive for the location  $(X, Y)$  of an eddy's centroid<sup>1</sup>:

$$\Pi X_{tt} - Y_t = \mathbf{L}_R^1 T \beta \langle yv \rangle + L \frac{\beta}{f} \langle y\eta v \rangle \quad (3.1)$$

$$\Pi Y_{tt} - X_t = -\mathbf{L}_R^1 T \beta \langle yu \rangle - L \frac{\beta}{f} \langle y\eta u \rangle \quad (3.2)$$

where  $\Pi = 1/f_0 T$ .

Hence, independent of balance of forces the eddy's center of mass describes inertial oscillations<sup>2</sup> on the  $f$ -plane, even in the absence of  $\beta$ . Using geostrophic values for  $u$  and returning to dimensional variables equation (3.1) can be cast into:

$$\begin{aligned} \frac{\partial X}{\partial t} &= -\frac{\beta g' \int_A H\eta \, dA + \int_A \eta^2/2 \, dA}{\int_A \eta \, dA} \\ &= -\beta \left( \frac{NH}{f_0} \right)^2 - \frac{\int_A \eta^2/2 \, dA}{\int_A \eta \, dA} \quad (3.3) \\ &= \frac{\partial \omega_{long}}{\partial k} - u_{internal} \end{aligned}$$

THE first term of the RHS of equation (3.3) represents the *planetary lift*<sup>3</sup>, which is identical to the zonal group velocity of long Rossby waves (Cushman-Roisin, 2010). The second term  $u_{internal}$  represents the *eddy-internal  $\beta$ -effect* (see drift-speed-box 2.2.3). Note that the first term is always westwards, while the second has sign of  $-\eta$ , i.e. westward for anti-cyclones and eastward for cyclones and that the first is always much larger than the second.

<sup>1</sup>  $\langle \rangle \equiv \frac{1}{A} \int_A \, dA$ .

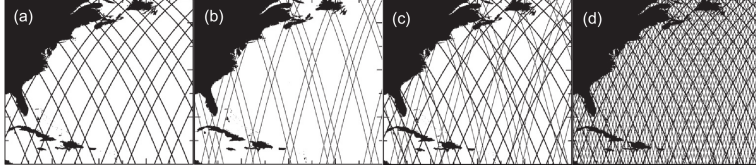
<sup>2</sup> compare to *harmonic oscillator*.

<sup>3</sup> see drift-speed-box 2.2.2 from section 2.2.

### Early Altimeter Data

THE advent of satellite altimetry, which Walter Munk called *the most successful ocean experiment of all time* (Munk, 2002), finally allowed for global-scale experimental investigations of oceanic planetary phenomena on long time- and space-scales. Among others, Matano *et al.* (1993); Cipollini *et al.* (1997); Le Traon & Minster (1993) were the first to use satellite data to present evidence for the existence of Rossby waves and their westward migration in accord with theory. Surprisingly all of the observations found the phase speeds to be 1 to 1.5 times larger than what theory predicted. Several theories to explain the discrepancy were presented. E.g. Killworth *et al.* (1997) argued that the discrepancy was caused by mode-2-east-west-mean-flow velocities. Interestingly it appears that hitherto, the relevant altimeter signal was mainly associated

with linear waves. Non-linearities are rarely mentioned in the papers of those years. Probably simply due to the fact that the turbulent character of much of the mesoscale variability was still obscured by the poor resolution of the first altimeter products.



### SSH Altimeter Data ([Chelton et al. , 2007, 2011](#))

From the beginning of satellite altimetry [Chelton et al.](#) have invested tremendous effort to thoroughly analyze the data in terms of Rossby waves and geostrophic turbulence. At the time of the [Killworth et al. \(1997\)](#) paper only 3 years of Topex/Poseidon data alone had been available, which led them to interpret the data mainly in terms of Rossby waves. Once the merged Aviso T/P and ERS 1/2 ([Forget, 2010](#)) was released 7 years later, [Chelton et al.](#) presented a new analysis that was based on an automated eddy-tracking algorithm using the geostrophic Okubo-Weiss parameter<sup>4,5</sup>. For the first time satellite data was resolved sufficiently fine to unveil the dominance of *blobby structures rather than latitudinally  $\beta$ -refracted continuous crests and troughs* that had hitherto been assumed to characterize the large-scale SSH topography. They presented results of a refined algorithm in their [2011](#) paper, in which they abandoned the Okubo-Weiss concept and instead identified eddies via closed contours of SSH itself. The improved algorithm and longer data record now allowed them to separate the non-linear eddy activity from the larger-scale Rossby waves. They find that the vast majority of extra-tropical westward propagating SSH variability does indeed consist of coherent, isolated, non-linear, mesoscale eddies that propagate about 25% slower<sup>6</sup> than the linear waves. Apart from this though they find little evidence for any dispersion in the signal, neither do they find evidence for significant meridional propagation, as should be found for Rossby waves ([Olbers et al. , 2012](#), chapter 8.2.1). In agreement with [Rhines & Holland \(1979\)](#), they find this eddy-dominated regime to fade towards the equator, giving way to the characteristic Rossby wave profile. Almost all of their eddies propagate westwards. Those eddies that are advected eastwards by e.g. the ACC show significantly shorter life-times than those that are not. For more detail on their results and a discussion of the limitations of eddy-tracking via satellites (see

Figure 3.1: The ground track patterns for the 10-day repeat orbit of T/P and its successors Jason-1 and Jason-2 (thick lines) and the 35-day repeat orbit of ERS-1 and its successors ERS-2 and Envisat (thin lines). (a) The ground tracks of the 10-day orbit during a representative 7-day period; (b) The ground tracks of the 35-day orbit during the same representative 7-day period; (c) The combined ground tracks of the 10-day orbit and the 35-day orbit during the 7-day period; and (d) The combined ground tracks of the 10-day orbit and the 35-day orbit during the full 35 days of the 35-day orbit. (sic) ([Chelton et al. , 2011](#))

<sup>4</sup> see section 2.1.

<sup>5</sup> see [derivation 5](#)

<sup>6</sup> pointing to dispersion.

section 2.4).

## 4

### The Algorithm

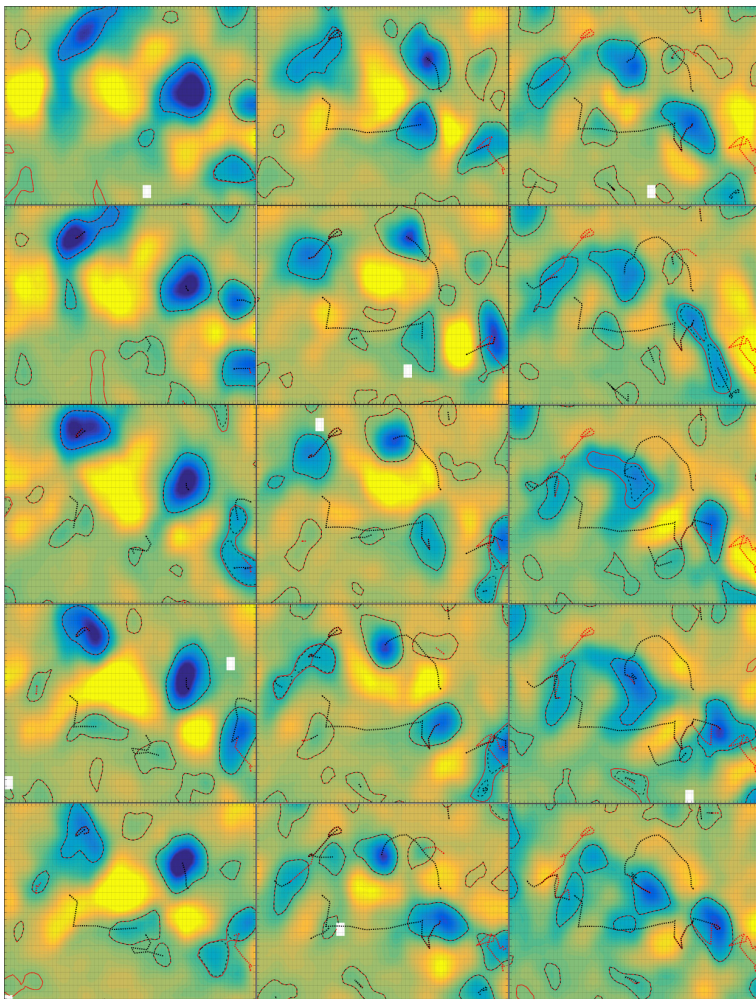


Figure 4.1: Fortnightly [Aviso-MII](#) snapshots (cyclones only) showing the area from  $47.6^{\circ}\text{S}$  to  $30.1^{\circ}\text{S}$  and  $40.1^{\circ}\text{E}$  to  $64.9^{\circ}\text{E}$ . Threshold age for saving is  $8 \times 7\text{days}$ . Red [black] color represents **MI** [**MII**]. Dashed lines are the contours and dotted lines are the tracks. Only *active* tracks are drawn. The general impression from animations of this sort is that the **MI**-method is good at tracking coherent, west-ward propagating, less-circular **SSH** anomalies while the **MII**-method seems superior at successfully tracking higher-amplitude vortices that get advected by mean currents (*e.g.* the strong cyclone in appr. the middle of the picture describing an anti-clockwise circular track due to advection by the ACC.)

THIS section walks through the algorithm step by step, so as to explain which methods are used and how they are implemented. The idea is that the code from step `s00..` on can only accept one particular structure of data. In earlier versions the approach was to write code that would adapt to different types of data automatically. All of this extra adaptivity turned out to

visually and structurally clog the code more than it did offer much of a benefit. The concept was therefore reversed. Input SSH-data needs to be altered to required format. Yet, there should be no need to adapt any of the later steps in any way. All input parameters are to be set in `INPUT.m` and `INPUTx.m`. A well-documented *core*-version (stripped of all experimental and redundant add-ons) will be made public on github presumably as early as end of June 2015 and no later than August 2015.

#### 4.1 Step Soo: Prepare Data

```
function S00_prep_data
```

BEFORE the actual eddy detection and tracking is performed, SSH-, latitude- and longitude grids are extracted from the given data at desired geo-coordinate bounds and saved as structures in the form needed by the next step (So1). This step also builds the file `window.mat` via `GetWindow3` which saves geometric information about the input and output data as well as a cross-referencing index-matrix which is used to reshape all *cuts* to the user-defined geo-coordinate geometry. The code can handle coordinate input that crosses the longitudinal seam of the input data. E.g. say the input data came in matrices that start and end on some (not necessarily strictly meridional) line straight across the Pacific and it is the Pacific only that is to be analyzed for eddies, the output maps are stitched accordingly. In the zonally continuous case *i.e.* the full-longitude case, an *overlap* in x-direction across the *seam*-meridian of the chosen map is included so that contours across the seam can be detected and tracked across it. One effect is that eddies in proximity to the seam can get detected twice at both zonal ends of the maps. The surplus double-eddies get filtered out in `S05_track_eddies`.

#### 4.2 Step So1b: Find Mean Rossby Radii and Phase Speeds

```
function S01b_BruntVaisRossby
```

THIS function...

- – ...calculates the pressure  $P(z, \phi)$  in order to...
- ...calculate the Brunt-Väisälä-Frequency according to  

$$N^2(S, T, P, \phi) = -\frac{g(\phi)}{P} \frac{\partial \rho(S, T, P)}{\partial z}$$
 in order to...
- – ...integrate the Rossby-Radius  $L_R^1 = \frac{1}{\pi f} \int_H N dz$  and ...
- apply the long-Rossby-Wave dispersion relation to  
 found  $L_R^1$  to estimate Rossby-Wave phase-speeds  $c = -\frac{\beta}{k^2 + (1/Lr)^2} \approx -\beta L_R^{1/2}$

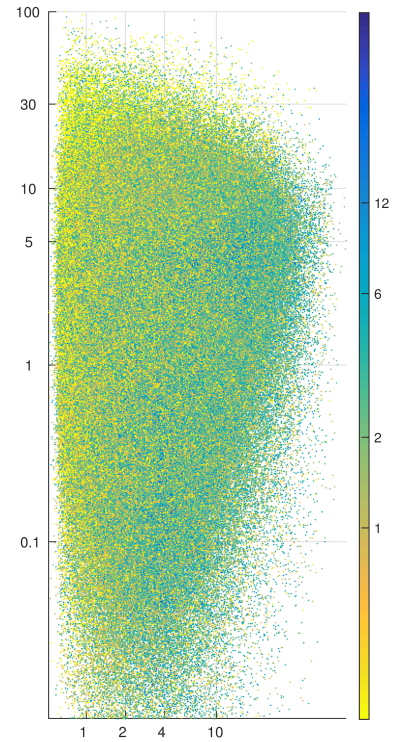


Figure 4.2: POP-7day-MII : Small amplitude correlates with a short life and a broad drift speed spectrum.  
y-axis: zonal drift speed [cm/s], x-axis: amplitude [cm], color: age [months].

The 3-dimensional matrices ( $S$  and  $T$ ) are cut zonally into slices which then get distributed to the threads. This allows for direct matrix operations for all calculations which would otherwise cause memory problems due to the immense sizes of the 3d-data<sup>1</sup>.

<sup>1</sup> E.g. the POP data has dimensions  $42 \times 3600 \times 1800$ .

### Step S02: Calculate Geostrophic Parameters

```
function S02_infer_fields
```

THIS step reads the cut **SSH** data from `s00_prep_data` to perform 2 steps:

1. Calculate a mean over time of  $SSH(y, x)$ .
2. • use one of the files' geo-information to determine  $f$ ,  $\beta$  and  $g$ .  
 • calculate geostrophic fields from **SSH** gradients.  
 • calculate deformation fields (vorticity, divergence, stretch and shear) via the fields supplied by the last step.  
 • calculate  $O_w$ .  
 • Subtract the mean from step 1 from each  $SSH(t)$  to filter out persistent SSH-gradients e.g. across the Gulf-Stream.

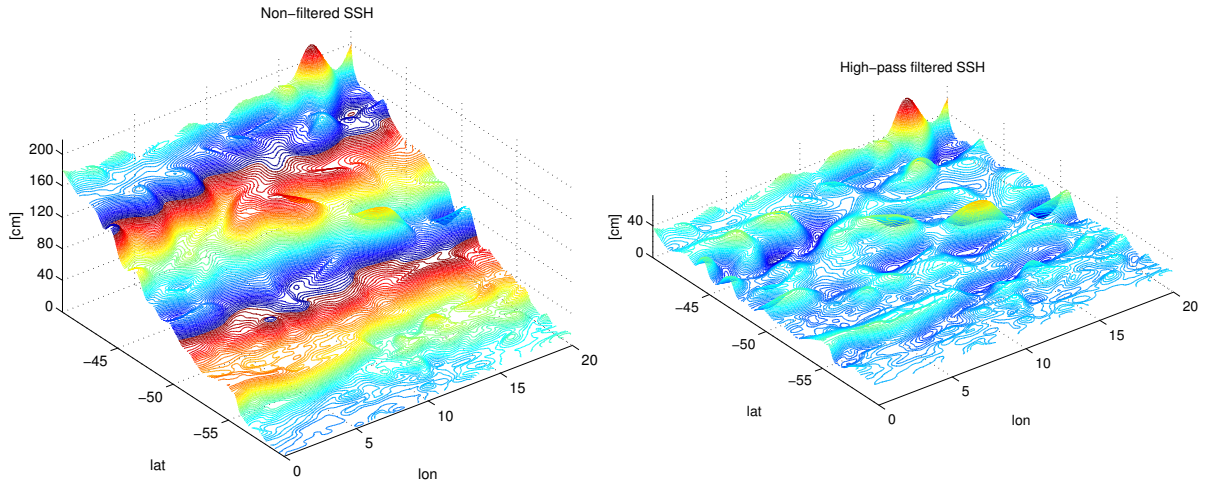


Figure 4.3: SSH with mean over time subtracted.

### 4.3 Step S03: Find Contours

```
function S03_contours
```

THE sole purpose of this step is to apply MATLAB's `contourc.m` function to the **SSH** data. It simply saves one file per time-step with all contour indices appended into one vector<sup>2</sup>. The

<sup>2</sup> see the MATLAB documentation.

contour intervals are determined by the user defined increment and range from the minimum- to the maximum of given **SSH** data.

The function `initialise.m`, which is called at the very beginning of every step, here has the purpose of rechecking the *cuts* for consistency and correcting the time-steps accordingly (*i.e.* when files are missing). `initialise.m` also distributes the files to the threads *i.e.* parallelization is in time dimension.

#### 4.4 Step S04: Filter Contours

```
function S04_filter_eddies
```

SINCE indices of all possible contour lines at chosen levels are available at this point, it is now time to subject each and every contour to a myriad of tests to decide whether it qualifies for the outline of an eddy as defined by the user input threshold parameters.

##### 4.4.1 Reshape for Filtering and Correct out of Bounds Values

```
function eddies2struct
function CleanEddies
```

In the first step the potential eddies are transformed to a more sensible format, that is, a structure `Eddies` of size `EddyCount`. The struct has fields for level, number of vertices, exact *i.e.* interpolated coordinates and rounded integer coordinates.

The interpolation of `contourc.m` sometimes creates indices that are either smaller than 0.5 or larger than<sup>3</sup>  $N + 0.5$  for contours that lie along a boundary. After rounding, this seldomly leads to indices of either 0 or  $N + 1$ . These values get set to 1 and  $N$  respectively in this step.

<sup>3</sup> where  $N$  is the domain size.

##### 4.4.2 Descend/Ascend Water Column and Apply Tests

```
function walkThroughContsVertically
```

The concept of this step is a direct adaptation of the algorithm described by Chelton *et al.* (2011). It is split into two steps, one for anti-cyclones and one for cyclones. Consider *e.g.* the anti-cyclone situation: Since all geostrophic anti-cyclones are regions of relative high pressure, all **ACs** effect an elevated **SSH** *i.e.* a *hill*. The algorithm ascends the full range of **SSH** levels where contours were found. Consider next an approximately Gaussian shaped **AC** that has a peak **SSH** of say 5 increments larger than the average surrounding waters. As the algorithm approaches the sea surface from below, it will eventually run into contours that are closed onto themselves and that encompass the **AC**. At first these contours might be

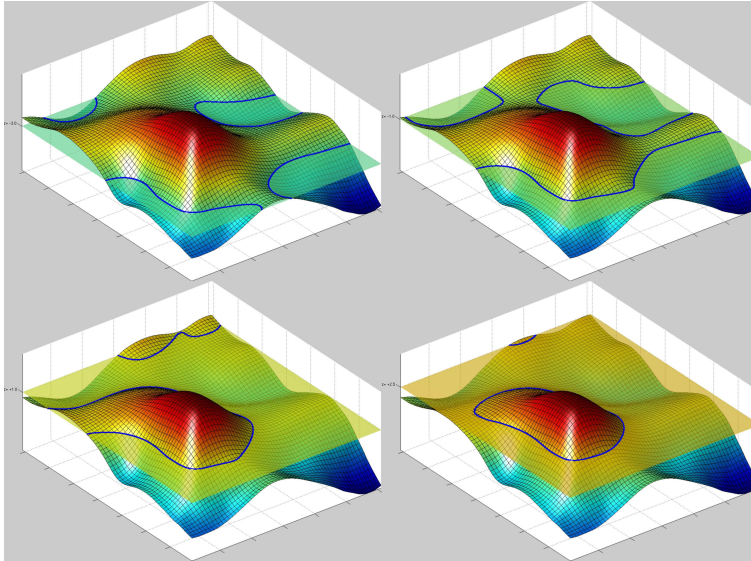


Figure 4.4: The algorithm approaches the appropriate vertical level incrementally.

very large and describe not only one but several ACs and likely also cyclones, but as the algorithm continues upwards, found contour will get increasingly circular, describing some outer edge of the AC. Once the contour and its interior pass all of the tests, the algorithm will decide that an AC was found and write it and all its parameters to disk. The AC's region *i.e.* the interior of the contour will be flagged from here on. Hence any inner contour further up the water column will not pass the tests. Once all ACs are found for a given time-step, the SSH flags get reset and the entire procedure is repeated, only this time *descending* the SSH-range to find cyclones. The tests for cyclones and anti-cyclones are therefor identical except for a factor  $-1$  where applicable. In the following the most important steps of the analysis are outlined.

#### **Contour filter 1 NaN-Check Contour**

```
function CR_RimNan
```

The first and most efficient test is to check whether indices of the contour are already flagged. Contours within an already found eddy get thereby rejected immediately.

#### **Contour filter 2 Closed Ring**

```
function CR_ClosedRing
```

Contours that do not close onto themselves are obviously not eligible for further testing.

#### **Contour filter 3 Sub-Window**

```
function get_window_limits, EddyCut_init
```

For further analysis a sub-domain around the eddy is cut out of the SSH data. These functions determine the indices of that window and subtract the resultant offset for the contour

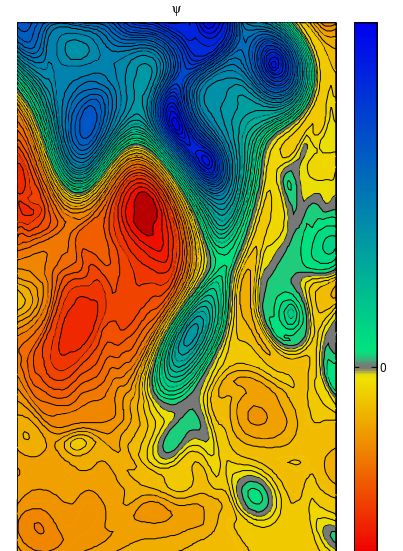


Figure 4.5: Stream function of a meandering jet shedding off a vortex. The line of strongest gradient *i.e.* fastest geostrophic speed later becomes the zero-vorticity-line at a theoretical distance  $\sigma$  from the center (Offset of  $\Psi$  is chosen arbitrarily).

indices.

#### Contour filter 4 Logical Mask of Eddy Interior

```
function EddyCut_mask
```

Basically this function creates a **flood-fill** logical mask of the eddy-interior. This is by far the most calculation-intensive part of the whole filtering procedure. A lot more time was wasted on attempting to solve this problem more efficiently than time could have been saved would said attempts have been successful. The current solution is basically just MATLAB's `imfill.m`, which was also used in the very first version of 09/2013. EDIT: `imfill.m` was replaced by using `inpoly.m` to determine which indices lie within the contour-polygon. This method seems to be more exact at determining whether the inside-part of one grid cell (with respect to the smooth, spline-interpolated contour) is larger than the outside part or not.

#### Contour filter 5 Sense

```
function CR_sense
```

All of the interior **SSH** values must lie either above or below current contour level, depending on whether anti-cyclones or cyclones are sought.

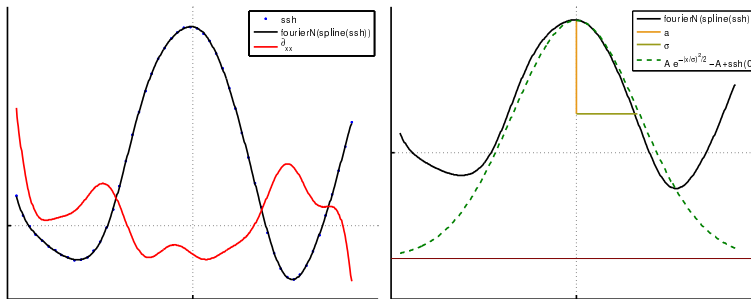


Figure 4.6: Left: Fourier-fit of an eddy from POP SSH-data and the 2nd derivative thereof. Right: Theoretical Gauss shape built from the resulting *standard-deviation i.e.  $\sigma$*  and amplitude.

#### Contour filter 6 Area

```
function getArea
```

The main goal here is to determine the area encompassed by the interpolated coordinates of the contour. It does so via MATLAB's `polyarea` function. This area is not related to the scale  $\sigma$  that is determined in contour-filter 12. It is however the relevant scale for the determination of the isoperimetric quotient in contour-filter 8.

If the respective switch is turned on, this function also checks that the area of found contour does not surpass a given threshold which in turn is a function of  $L_R^1$ . Since  $L_R^1$  gets very small in high latitudes a lower bound on the  $L_R^1$  used here should be set as well. This is especially important for the southern ocean where  $L_R^1$  gets very small while the strong mesoscale turbulence of the Antarctic circumpolar current

results in an abundance of relatively large eddies as far south as 60°S and beyond.

### Contour filter 7 Circumference

`function EddyCircumference`

Circumference e.g. line-length described by the contour. This is the other parameter needed for contour-filter 8. This is however neither related to the actual eddy scale determined in contour-filter 12.

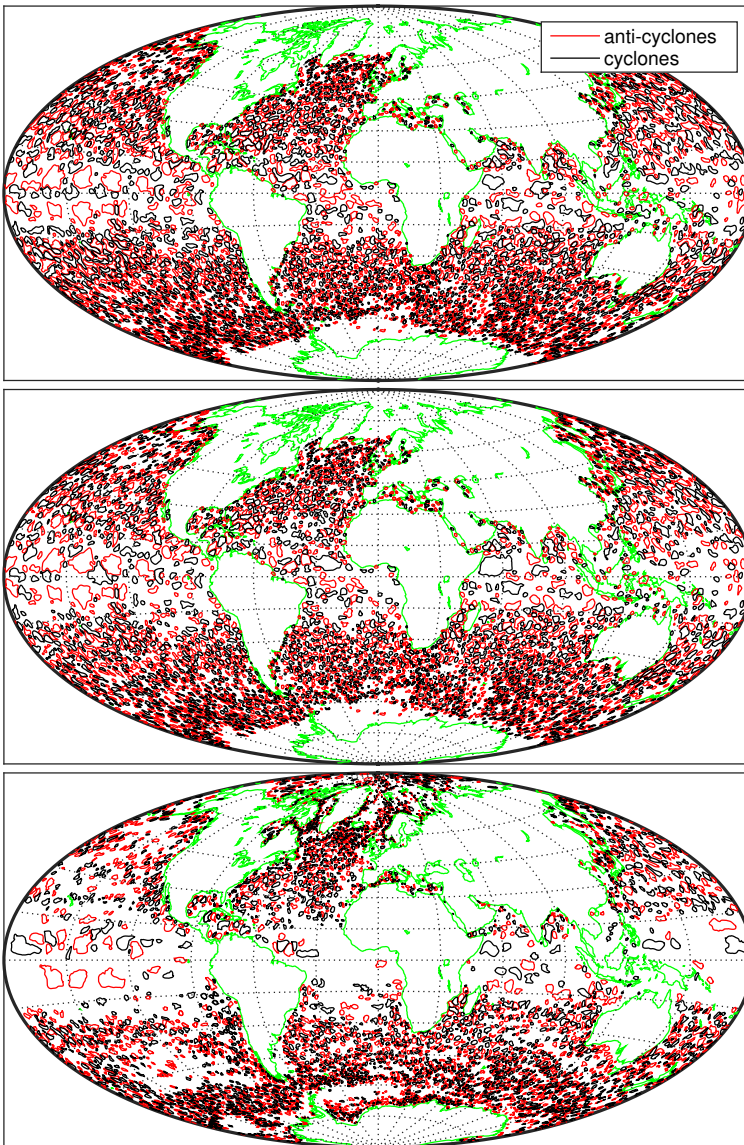


Figure 4.7: All contours that passed the filtering procedure for one exemplary time-step. Top: Aviso-MI . Mid: Aviso-MII . Bottom: POP-7day-MII .

### Contour filter 8 Shape

`function CR_Shape`

This is the crucial part of deciding whether the object is *round enough*. A perfect vortex with  $\frac{\partial u}{\partial y} = -\frac{\partial v}{\partial x}$  is necessarily a circle. The problem is that eddies get formed, die, merge, run into

obstacles, get asymmetrically advected etc. To successfully track them it is therefore necessary to allow less circle-like shapes whilst still avoiding to e.g. count 2 semi-merged eddies as one.

This is achieved by calculating the **isoperimetric quotient**, defined as the ratio of a ring's area to the area of a circle with equal circumference. Chelton *et al.* (2011) use a similar method. They require:

*The distance between any pair of points within the connected region must be less than a specified maximum (Chelton *et al.*, 2011).*

While this method clearly avoids overly elongated shapes it allows for stronger deformation within its distance bounds.

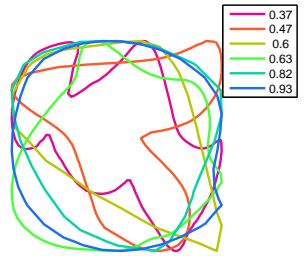


Figure 4.8: Different values of the isoperimetric quotient.

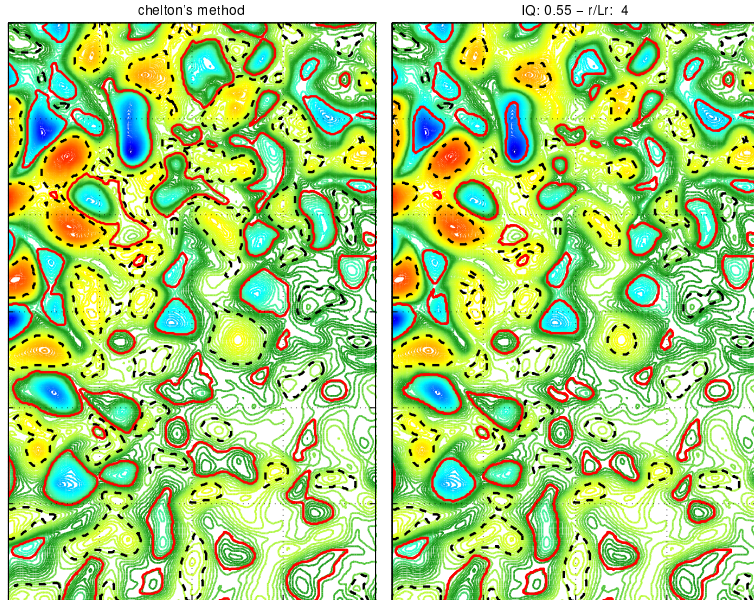


Figure 4.9: Left: The Chelton-method expects to detect eddies at their base and is rather tolerant with respect to the shape of found contour. The IQ-method aims more at detecting single round vortices without expecting found contour to be necessarily related to any howsoever-defined outer edge of the eddy.

### Contour filter 9 Amplitude

```
function CR_AmpPeak
```

This function determines the amplitude *i.e.* the maximum of the absolute difference between **SSH** and current contour level and the position thereof as well as the amplitude relative to the mean **SSH** value of the eddy interior as done by Chelton *et al.* (2011). The amplitude is then tested against the user-given threshold. The function also creates a matrix with current contour level shifted to zero and all values outside of the eddy set to zero as well.

### Contour filter 10 Chelton's Scales

```
function cheltStuff
```

Chelton *et al.* (2011) introduced 4 different eddy-scales.

1. The effective scale  $L_{eff}$  as the radius of a circle with its area equal to that enclosed by the contour.

2. The scale  $L_e$  as the radius at  $z = e^{-1}a$  with  $a$  as the amplitude with reference to the original contour and the  $z$ -axis zero-shifted to that contour. In other words the effective scale of the contour that is calculated at  $1/e$  of the original amplitude.
3. The scale  $L = L_e/\sqrt{2}$ .
4. The scale  $L_s$  which is a direct estimate based on the contour of SSH within the eddy interior around which the average geostrophic speed is maximum (Chelton et al., 2011). It is hence conceptually the same as  $\sigma$ . This scale was not calculated here, as I could not think of an efficient, simple way to estimate the area bounded by maximum geostrophic speed i.e. the zero-vorticity contour. To understand why this would be difficult to achieve see also contour-filters 11 and 12 and section 2.4.

### Contour filter 11 Profiles

```
function EddyProfiles
```

This step

- saves the meridional and zonal profiles of SSH, U and V through the Eddy's peak, spanning the entire sub-domain as described in contour-filter 4.
- creates spline functions from the ssh-profiles and uses them to interpolate the profiles onto 100-piece equi-distant coordinate vectors to build smooth interpolated versions of ssh-profiles in both directions.
- in turn uses the splined data to create smooth 4-term Fourier series functions for the profiles.

### Contour filter 12 Dynamic Scale ( $\sigma$ )

```
function EddyRadiusFromUV
```

The contour line that is being used to detect the eddy is not necessarily a good measure of the eddy's scale i.e. it doesn't necessarily represent the eddy's outline very well. This becomes obvious when the area, as inferred by contour-filter 6, is plotted over time for an already successfully tracked eddy. The result is not a smooth curve at all. This is so because at different time steps the eddy usually gets detected at different contour levels. Since its surrounding changes continuously and since the eddy complies with the testing-criteria the better the closer the algorithm gets to the eddy's peak value, the determined area of the contour jumps considerably between time steps. This is especially so for large flat eddies with amplitudes on the order of 1cm. If the contour increment is on that scale as well, the difference in contour-area between two time steps

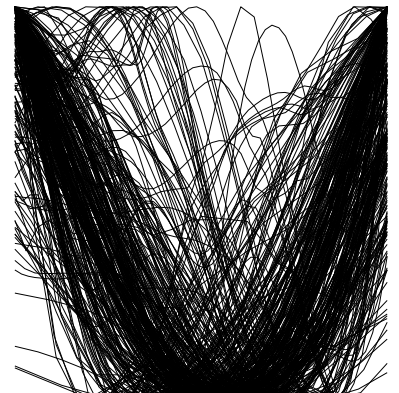
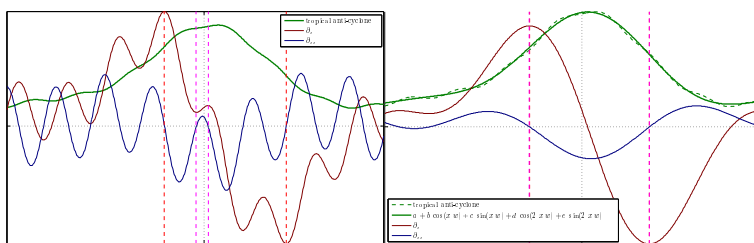


Figure 4.10: Zonal x- and z-normalized cyclone-profiles (early data ~'13/12).

easily surpasses 100% and more. Since there is no definition for the *edge* of an eddy, it is defined here as the ellipse resulting from the meridional [zonal] diameters that are the distances between the first local extrema of orbital velocity (one negative, one positive) away from the eddy's peak in  $y$ - [ $x$ -] direction<sup>4</sup>. In the case of a meandering jet with a maximum flow speed at its center, that is shedding off an eddy, this scale corresponds to half the distance between two opposing center-points of the meander. It is also the distance at which a change in vorticity-polarity occurs and is thus assumed to be the most plausible dividing line between vortices. Trying to determine the location where this sign change in vorticity occurs in the profiles turns out to be very tricky. What we seek are local extrema of the geostrophic speeds *i.e.* of the SSH-gradients  $h_x$ . In a perfect Gaussian-shaped eddy, these would simply correspond to the first local extrema of  $h_x$  away from the peak. In *reality* the eddies can be very wobbly with numerous local maxima and minima in the gradients of their flanks. One could argue, that it must be the largest extrema, as it is the highest geostrophic speeds that are sought. In practice<sup>5</sup>, multiple superimposed signals of different scales often create very strong gradients locally. But the main issue here is that one weak eddy adjacent to one strong eddy also has the stronger gradients of the stronger one within its domain so that simply looking for the fastest flow speeds along the profiles is insufficient. It is also not possible to restrict the cut domain to the extent of a single eddy only, because at the time when the domain is selected, we do not know yet whether the detection algorithm *took bait* at the eddy's base or later close to the tip.

The best method thus far seems to be to use the Fourier-series functions from contour-filter 11 to determine the first extrema away from the eddy's peak (see fig. 4.11). The Fourier order was chosen to be 4 by trial and error. The effect is that small-scale low-amplitude noise is avoided, allowing for more reliable determinations of  $\nabla^2 h_{\text{fourier}} = 0$ .

Once the zero crossings in all 4 directions are found, their mean is taken as the eddy's scale ( $\sigma$ ).



<sup>4</sup> The velocities are calculated from the gradients of 4th-order Fourier fits to the SSH profile in respective direction (see contour-filter 11).

<sup>5</sup> Especially for the high-resolution model data.

Figure 4.11: A flat wobbly low-latitude eddy resulting in multiple zero-crossings of its  $\nabla^2$ . The problem is addressed by differentiating the profile's Fourier-Series fit instead.

### Contour filter 13 Dynamic Amplitude

```
function EddyAmp2Ellipse
```

As mentioned above, the contour that helps to detect the eddy is not representative of its extent. This is also true for the  $z$ -direction, for the same reasons. This function therefor takes a **SSH-mean** at indices of the ellipse spun by the determined zonal and meridional *dynamical* diameters, and uses this as the basal value to determine a *dynamic* amplitude.

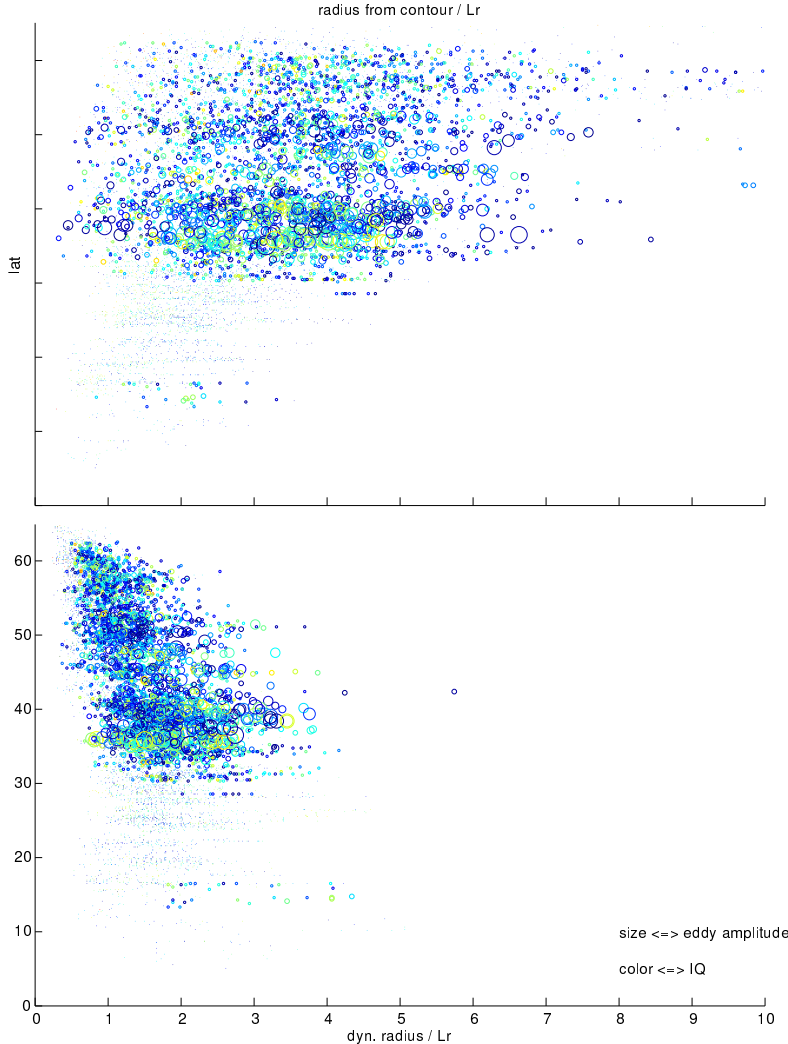


Figure 4.12: Eddies in the North-Atlantic. Y-axis: latitude. X-axis top: ratio of radius of circle with equal area to that of found contour to local Rossby-radius. X-axis bottom: ratio of  $\sigma$  to local Rossby-radius. Color-axis: Isoperimetric Quotient (from blue to red). Size: amplitude. The bottom plot suggests that a ratio of say 4 for  $\sigma/L_R^1$  should be a reasonable threshold.

### Contour filter 14 Center of Volume (CoV)

```
function CenterOfVolume
```

Instead of using the geo-position of the eddy's peak in the tracking procedure, it was decided to instead use the center of the volume created by the basal shifted matrix from contour-filter 9 i.e. the center of volume of the dome (resp. valley) created by capping off the eddy at the contour level. This method was chosen because from looking at animations of the tracking procedure it became apparent that, still using peaks as reference points,

the eddy sometimes jumped considerably from one time step to the next if two local maxima existed within the eddy. E.g. in one time-step local maximum  $A$  might be just a little bit larger than local maximum  $B$  and one time-step later a slight shift of mass pushes local maximum  $B$  in pole position, creating a substantial jump in the eddy-identifying geo-position hence complicating the tracking procedure.

### *Contour filter 15 Geo Projection*

```
function ProjectedLocations
```

An optional threshold on the distance an eddy is allowed to travel over one time-step is implemented in the tracking algorithm in section 4.4. This is a direct adaptation of the ellipse-based constraint described by [Chelton et al. \(2011\)](#). The maximum distance in western direction traveled by the eddy within one time-step is limited according to  $x_{west} = \alpha c \delta t$  with  $c$  as the local long-Rossby-wave phase-speed and

e.g.  $\alpha = 1.75$ . In eastern direction the maximum is fixed to a value of e.g.  $x_{east} = 150\text{km}$ . This value is also used to put a lower bound on  $x_{west}$  and for half the minor axis ( $y$ -direction) of the resultant ellipse.

This function builds a mask of eligible geo-coordinates with respect to the next time-step.

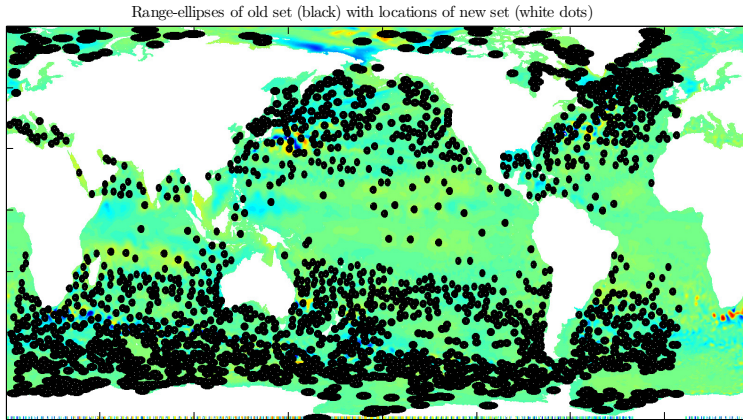


Figure 4.13: Among the saved meta-information for each eddy are also the indices describing the ellipse that defines the eddy's allowed locations for the next time-step.

## 4.5 Step S05: Track Eddies

```
S05_track_eddies
```

### 4.5.1 Main Tracking Procedure

DUE to the the fine temporal resolution (daily) of the model data, the tracking procedure for this case turns out to be much simpler than the one described by [Chelton et al. \(2007\)](#). There

is almost no need to project the new position of an eddy, as it generally does not travel further than its own scale in one day. This means that one eddy can usually<sup>6</sup> be tracked unambiguously from one time step to the next as long both time-steps agree on which eddy from the *other* time-step is located the least distance away. The algorithm therefore simply builds an arc-length-distance matrix between all old and all new eddies and then determines the minima of that matrix in both directions *i.e.* one array for the new with respect to the old, and one for the old with respect to the new set. This leads to the following possible situations:

- Old and new agree on a pair. *I.e.* old eddy  $O_a$  has a closest neighbor  $N_a$  in the new set and  $N_a$  agrees that  $O_a$  is the closest eddy from the old set. Hence the eddy is tracked.  $N_a$  is  $O_a$  at a later time.
- $N_a$  claims  $O_a$  to be the closest, but  $N_b$  makes the same claim. *I.e.* two eddies from the new set claim one eddy from the old set to be the closest. In this situation the closer one is decided to be the old one at a later time-step and the other one must be a newly formed eddy.
- At this point all new eddies are either allocated to their respective old eddies or assumed to be *newly born*. The only eddies that have not been taken care of are those from the old set, that *lost* ambiguity claims to another old eddy, that was closer to the same claimed new eddy. *I.e.* there is no respective new eddy available which must mean that the eddy just *died*. In this case the entire track with all the information for each time step is archived as long as the track-length meets the threshold criterion. If it doesn't, the track is abandoned.

#### 4.5.2 Improvements

The former is the core of the tracking algorithm. It is almost sufficient by itself as long as the temporal resolution is fine enough. The larger the time-step, the more ambiguities arise, which are attempted to be mitigated by flagging elements of the distance matrix not meeting certain thresholds:

- `function checkDynamicIdentity`  
Consider the ambiguous case when there are two new eddies  $N_a$  and  $N_b$  in sufficient proximity to old eddy  $O_a$ . Let's assume  $O_a$  is a relatively solid eddy of rel. large scale with a steep slope *i.e.* large amplitude and that  $N_a$  is merely a subtle blob of an eddy whilst  $N_b$  is somewhat similar to  $O_a$  but with only half the amplitude. The situation then is clear:  $N_b$  is the, apparently slowly dying,  $O_a$  at a later time,

<sup>6</sup> The only exception being the situation when one eddy fades and another emerges simultaneously and in sufficient proximity.

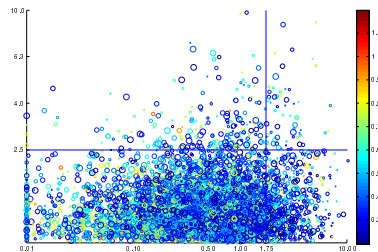


Figure 4.14: Each circle represents one eddy in the new time step. Y-axis: Maximum ratio to closest eddy in old set of either amplitude or  $\sigma$ , where 1 means *identical* and 2 means factor 2 difference. The threshold used for the final runs was 2. X-axis: Ratio of distance to closest eddy from old set divided by  $\delta t$  to local long-Rossby-wave phase-speed. Color-axis: Isoperimetric Quotient. Radius of circles: ratio of  $\sigma$  to local Rossby-radius. All eddies with said ratio larger than 10 are omitted. Note the obvious inverse correlation of scale to IQ, suggesting that all large *eddies* likely represent more than one vortex.

while  $N_a$  could either be a newly formed eddy, an old eddy with its respective representation in the old set something other than  $O_a$ , or even just temporary coincidental noise not representative of any significant mesoscale vortex at all. This interpretation should hold even when  $O_a$  sat right between the other two, thereby being much closer to  $O_a$  than  $N_b$  was. The purpose of this step is to make such decisions. It does so by comparing the *dynamic* versions of amplitude and scale (*ampToEllipse* and  $\sigma$ ) between the time-steps. If either ratio from new to old<sup>7</sup> surpasses a given threshold, the pair is flagged as non-eligible. It is important to use the *dynamic* parameters rather than those stemming from the contour line, because as mentioned in contour-filter 12, the contour line itself and the eddy's geometric *character* are hardly correlated at all. One eddy can get detected at different  $z$ -levels from one time-step to the next, resulting in completely different amplitudes, scales and shapes with respect to the contour.

The initial idea was, by assuming Gaussian shapes, to construct a single dimensionless number representing an eddy's geometrical character built upon the contour-related amplitude- and scale values only. Since we have no information about the vertical position of a given contour with respect to assumed Gauss bell, this problem turned out to be intrinsically under-determined and hence useless. The method eventually used, which checks amplitude and scale separately is again very similar to that described by Chelton *et al.* (see Box box 2).

- `function` `nanOutOfBounds`

This is the second half of the prognostic procedure described in section 4.5. It simply flags all pairs of the distance matrix for which the index representing the *new* eddy's geographic location is not among the set of indices describing the ellipse<sup>8</sup> around respective *old* eddy.

<sup>7</sup> In order to compare in both directions equally:  $\exp(|\log(v_n/v_o)|)$  where  $v$  is either amplitude or scale.

- `function` `checkAmpAreaBounds`

This is the direct adaptation of Chelton *et al.*'s description of how to test for sufficient similarity of amplitude and area between time steps.

<sup>8</sup> see figure fig. 4.13.

### Step S06: Cross Reference Old to New Indices

```
function S05_init_output_maps
```

The output Mercator-maps usually have different geometry from the input maps'. This step allocates all grid nodes of the input data to their respective nodes in the output map. Each output cell will then represent a mean of all input-nodes falling into that quadrilateral.

#### 4.6 *Running the Code*

THE separate steps can be run all at once (`Sall.m`) or one by one, as long as they are started consecutively in the order indicated by their name (`s00..`, then `s01..` etc.). Each step either creates its own output files or extends old ones, which are then read by the next step. All output data is saved in the user given root-path. This concept uses quite a lot of disk space and is also slowed substantially by all the reading and writing procedures. The benefit is that debugging becomes much easier. If the code fails at some step, at least all the calculations up to that step are dealt with and do not need to be re-run. The concept also makes it easier to extend the code by further add-ons and guarantees scalability.

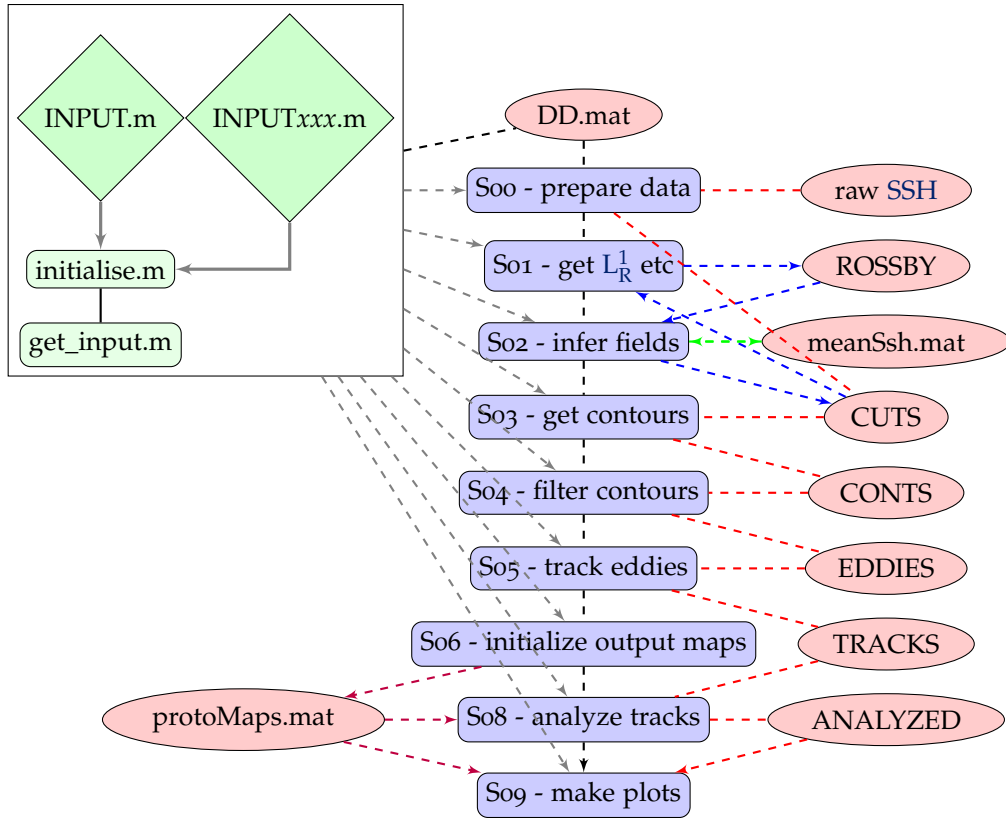


Figure 4.15: Basic code structure. The only files that are to be edited are the INPUT files. INPUT.m is independent of the origin of data, whilst the files INPUTaviso.m, INPUTpop.m etc set are samples of more source-specific parameter settings. Each of the SXx-steps initially calls initialise.m, which in turn scans all available data, reads in the INPUT data via get\_input.m, corrects for missing data etc and creates DD.mat. The latter is the main meta-data file, which gets updated throughout all steps. All data is built step-by-step along the consecutive SXx-steps (red line). The SXx-steps are the only programs that have to be called (in order) by the user. Beware that missing data (in time) is interpolated automatically in each step. Note also that meanSsh.mat should be recalculated if the time span is changed!

# 5

## Results

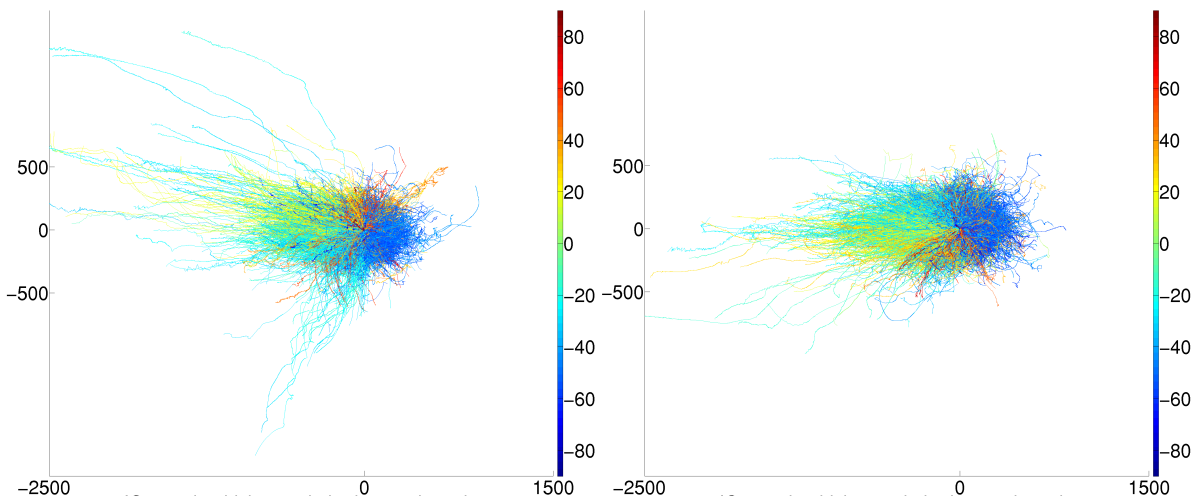


Figure 5.1: Baseline-shifted tracks. Left: anticyclones. Right: cyclones. Color represents *birth-latitude*. Thickness (hardly noticeable) represents *IQ*. Data is from a predecessor run to POP-7day-MII .

<sup>1</sup> depending on the number of CPU's and their frequencies.

<sup>2</sup> see fig. 4.7.

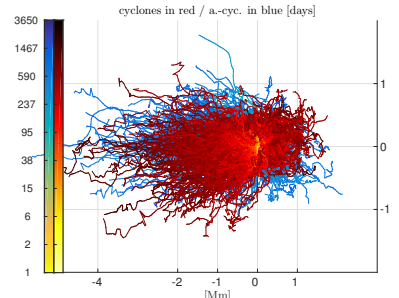


Figure 5.2: Aviso-MI : Baseline-shifted old ( $\text{age} > 500$  day) tracks. Cyclones in blue [days]. X/Y-axes are distance to birth place [1000km].

EVEN though all of the computer program's bottle-necks are parallelized in **SPMD**, an application to more than a decade of high-resolution **SSH** data still requires patience (say  $\mathcal{O}(10^1)$  -  $\mathcal{O}(10^2)$  days<sup>1</sup>). The most time-consuming of steps is the numerically arduous part of subjecting each of the vast number of found contours<sup>2</sup> to the filtering procedure as described in section 4.4. The total number of final analyses was hence limited and it was therefore critical to carefully choose which method/parameters to use in order to maximize the deducible insights from the results. For best comparability of the results with each other it was decided to agree on one complete set of parameters as a basis (table 5.1), which would then be altered at key parameters.

- The first run is an attempt to reproduce the results from Chelton *et al.* (2011). The **SSH**-data for this run is therefore that of the **Aviso** product. This method will be called **MI**.
- The second run (**MII**) is equivalent, except that this time the alternative **IQ**-based shape filtering method as described

in contour-filter 8 and the slightly different tracking-filter as described in section 4.5.2 are used. MII is then fed with 7-day time-step POP data as well.

- To investigate what role spatial resolution plays, the POP data was remapped to that of the Aviso data and fed to the MI method.
- Finally, to investigate the effects of resolution in time, an MII-2-day-time-step run over POP data was executed. For its results and discussion see section 6.2.
- Start and end dates were fix for all runs as the intersection of availability of both data sets.

#### Box 2: Method MI

The concepts used in this method are mostly based on the description of the algorithm described by Chelton *et al.* (2011) and all parameters are set accordingly. Basically MI is a modification of MII (which was completed first), with the aim to try to recreate the results from Chelton *et al.* (2011). It differs from MII in the following:

- **detection**

As mentioned in contour-filter 8, the approach by Chelton *et al.* (2011) is to avoid overly elongated objects by demanding:

- high latitudes

The maximum distance between any vertices of the contour must not be larger than  $400\text{km}$  for  $|\phi| > 25^\circ$ .

- low latitudes

The  $400\text{km}$ -threshold increases linearly towards the equator to  $1200\text{km}$ .

- **tracking**

The other minor difference to MII is in the way the tracking algorithm flags eddy-pairs between time-steps as sufficiently similar to be considered successful tracking-candidates (see section 4.5.2). In this method an eddy B from time-step  $k + 1$  is considered as a potential manifestation of an eddy A from time-step  $k$  as long as both - the ratio of amplitudes (with regard to the mean of SSH within the found contour) and the ratio of areas (interpolated versions as discussed in contour-filter 6) fall within a lower and an upper bound.

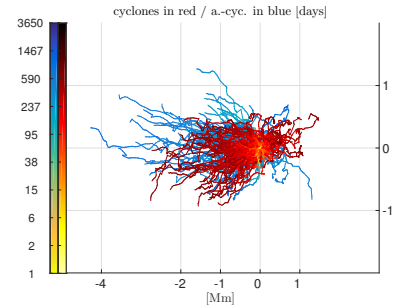


Figure 5.3: Aviso-MII : (same as fig. 5.2)

time frame	1994/01/05 - 2006/12/27
scope	$80^\circ\text{S}$ to $80^\circ\text{N}$ / full zonal.
Aviso geometry	641x1440 true Mercator
POP geometry	2400x3600 mixed proj.
contour step	0.01 m
<b>thresholds</b>	
max $\sigma/L_R^1$	4
min $L_R^1$	$20 \times 10^3$ m
min IQ	0.55
min number of points comprising found contour	8
max(abs(Rossby phase speed))	$1 \text{ m s}^{-1}$
min amplitude	0.01 m

Table 5.1: Fix parameters for all runs.

### Box 3: Method MII

The purpose of this variant is basically to test the conceptually different approach of using the **isoperimetric quotient** to judge the shape of found contour-rings as sufficiently eddy-*typical*. It also uses a slightly different tracking algorithm.

- **detection**

The **IQ**-method. See figs. 4.9, 6.2 and 6.3 and contour-filter 8.

- **tracking**

Conceptually similar to **MI**, it is again vertical and horizontal scales that are compared between time-steps.

Preferring a single threshold-value over one upper and one lower bound, a parameter  $\xi$  was introduced that is the maximum of the two values resulting from the two ratios of amplitude respective  $\sigma$ , where either ratio is -if larger- its reciprocal in order to equally weight a decrease or an increase in respective parameter. In other words:  $\xi = \max([\exp|\log R_\alpha|; \exp|\log R_\sigma|])$ , where  $R$  are the ratios.

## 5.1 MI - 7 day time-step - Aviso

THE RESULTS from the **MI** method are special in that they feature many long-lived eddies (see figs. 5.2, 5.7 and 5.8), some of which traveled more than 4000 km west. Tracks were recorded throughout the entire world ocean with the only exceptions being an approximately 20°-wide stripe along the equator. The highest count of unique eddies is along the Antarctic Circumpolar Current<sup>3</sup> with counts of more than 60 individual eddy-visits per  $1^\circ \times 1^\circ$ -cell. Further eddy-rich regions are the western North-Atlantic throughout the Gulf-Stream and North-Atlantic Current, *Mozambique eddies* (Schouten *et al.*, 2003) at 20° South along the Mozambique coast, along the Agulhas Current and south of the Cup of Good Hope at  $\sim 40^\circ$ , along the coasts of Brazil, Chile and all along the Eastern, Southern and Western coasts of Australia (see fig. 5.4). Eddies appear and disappear throughout the world ocean. For long-lived solid eddies there is a tendency to emerge along western coasts (see fig. 5.9).

THE SCALE  $\sigma$  of tracked eddies is similar to that in Chelton *et al.* (2011), yet generally smaller in high latitudes and slightly larger in low latitudes (see fig. 5.17). It is larger than the first-

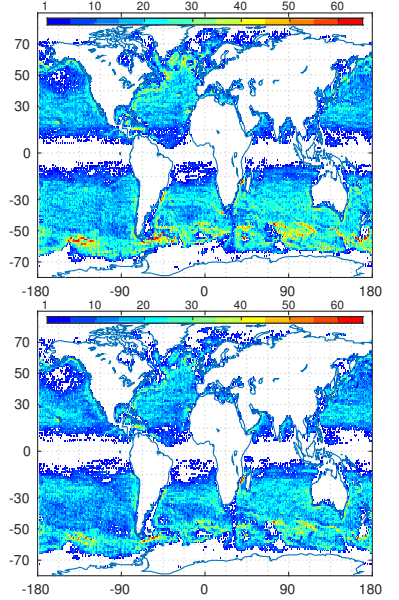


Figure 5.4: Top: **Aviso-MI**. Bottom: **Aviso-MII**. Total count of individual eddies per  $1^\circ$  degree square.

<sup>3</sup> abbreviated ACC from here on.

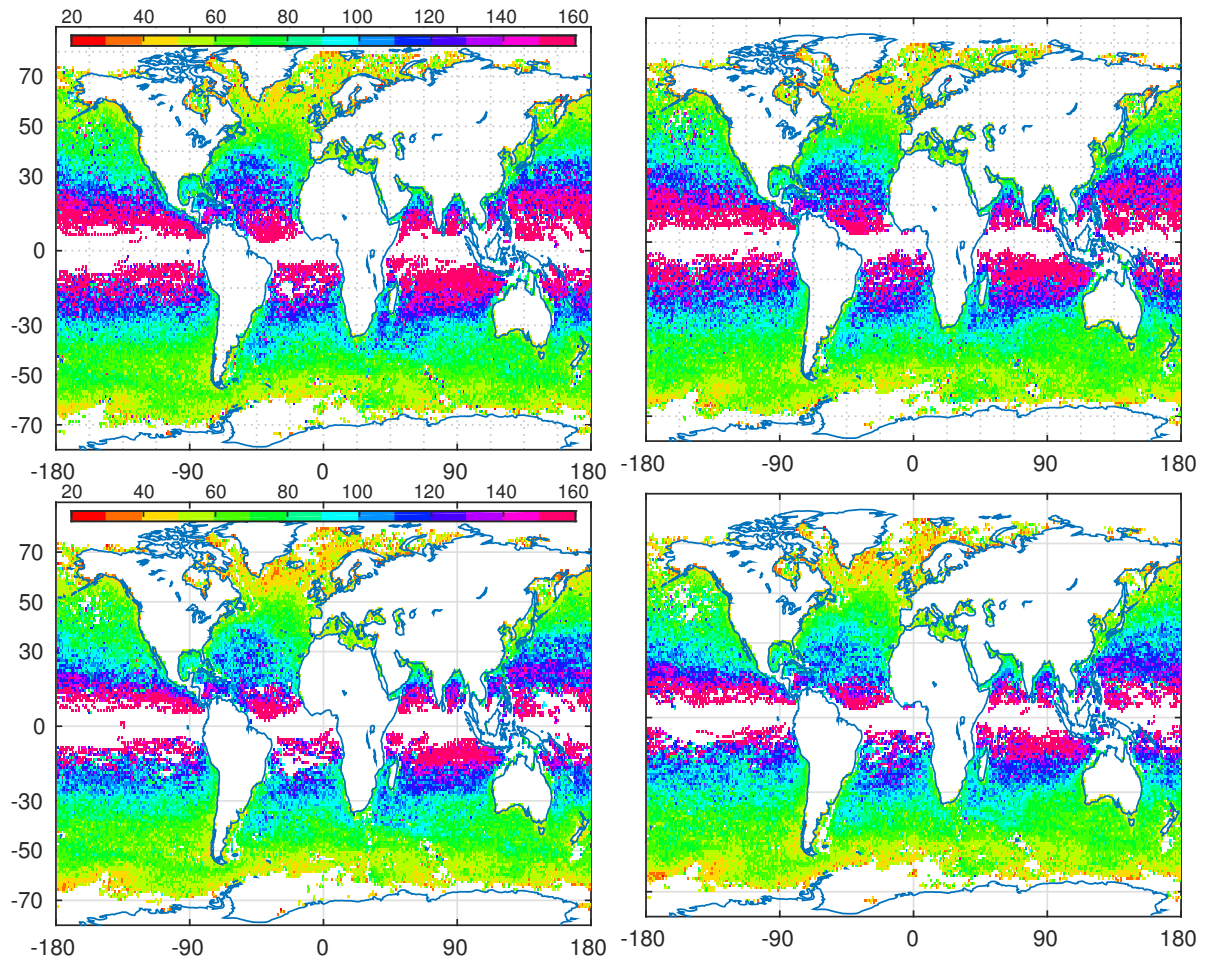


Figure 5.5: Top: Aviso-MI . Bottom  
Aviso-MII .  $\sigma$  [km]. Left: Anticyclones.  
Right: Cyclones.

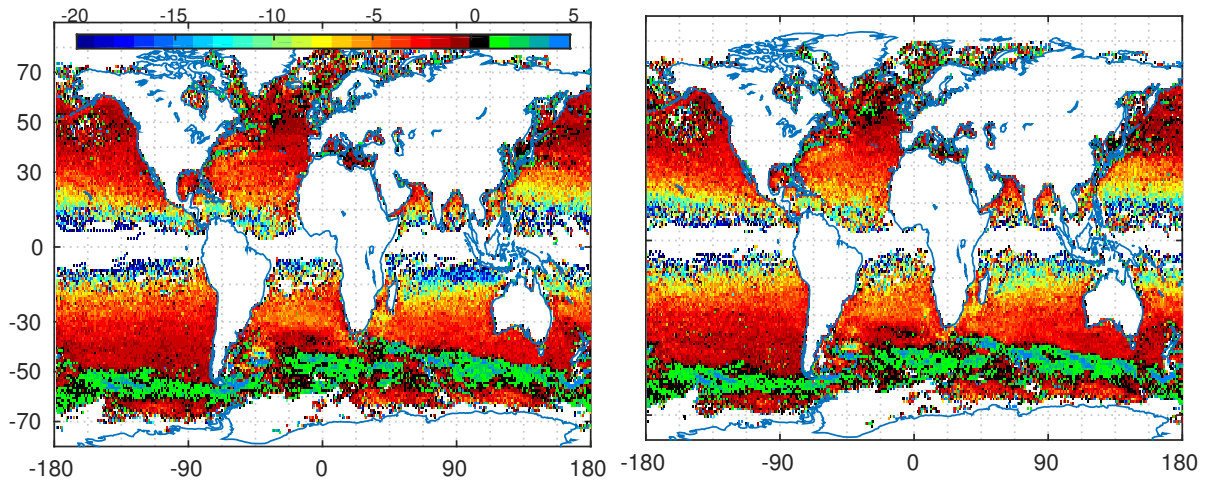


Figure 5.6: Aviso-MI : zonal drift  
speed [cm/s]. Left: Anticyclones.  
Right: Cyclones. Respective map for  
Aviso-MII not shown as it looks almost  
identical.

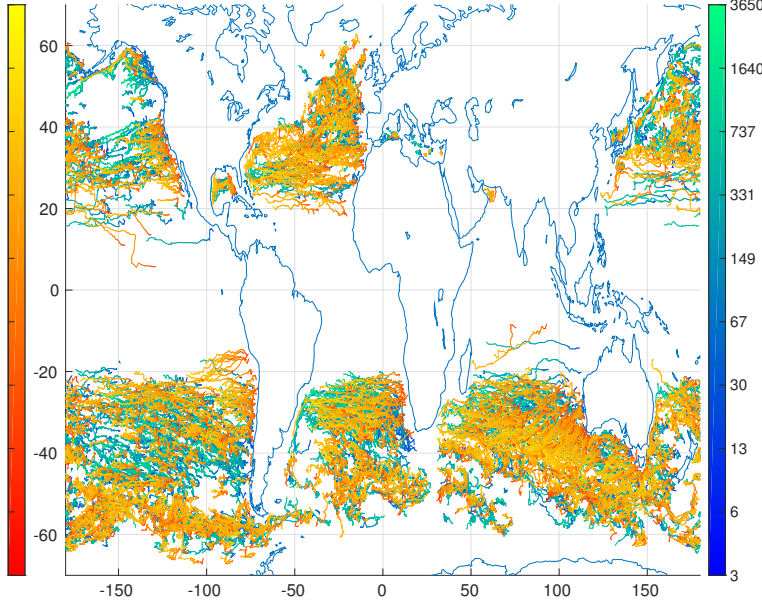


Figure 5.7: MI: Cyclones in red. Colors scale to eddy-age [days]. Both colorbars have the same scaling. Tracks younger than 1a omitted for clarity.

mode baroclinic Rossby Radius by a factor of at least 2 and its meridional profile appears to be separable into two different regimes; one apparently linear profile in low latitudes and a steeper one equator-wards of  $\sim |15^\circ|$ . Regionally, locations of high mesoscale activity appear to correlate with smaller eddy-scales (see fig. 5.5).

THE eastward zonal drift speeds are slightly slower than the first-mode long Rossby wave phase speed and agree well with the results from Chelton *et al.* (2011). Propagation is generally westwards except for regions of sufficiently strong eastward advection as in the ACC and North Atlantic Current (see figs. 5.6 and 5.17).

places of birth and death. size indicates final age.

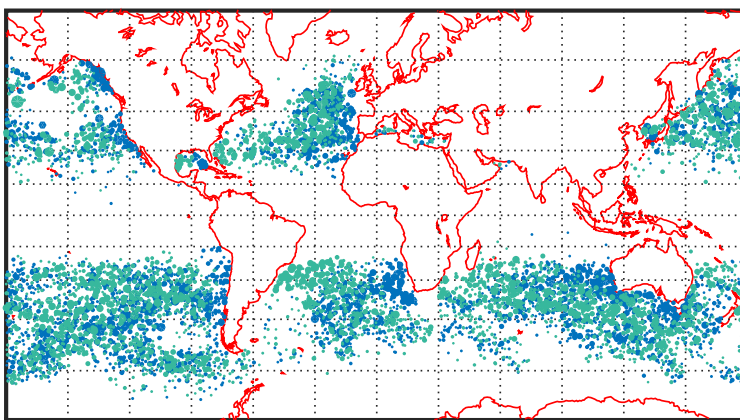


Figure 5.9: Aviso-MI : Births are in blue and deaths in green. Size of dots scales to age squared. Only showing tracks older than one year.

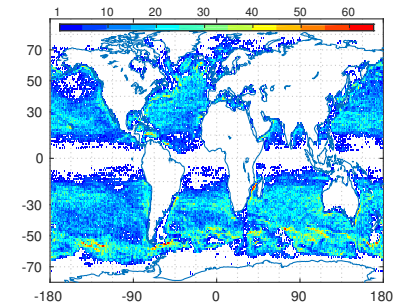


Figure 5.10: Aviso-MII : Total count of individual eddies per 1 degree square.

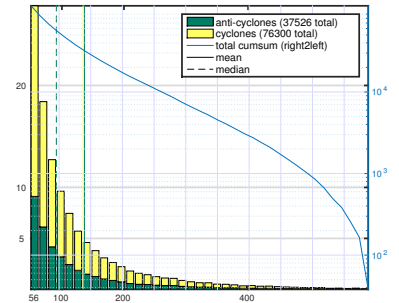


Figure 5.8: Aviso-MI : Final age distribution. x-axis: [days], Left y-axis: [1000]

## 5.2 MII - 7 day time-step - Aviso

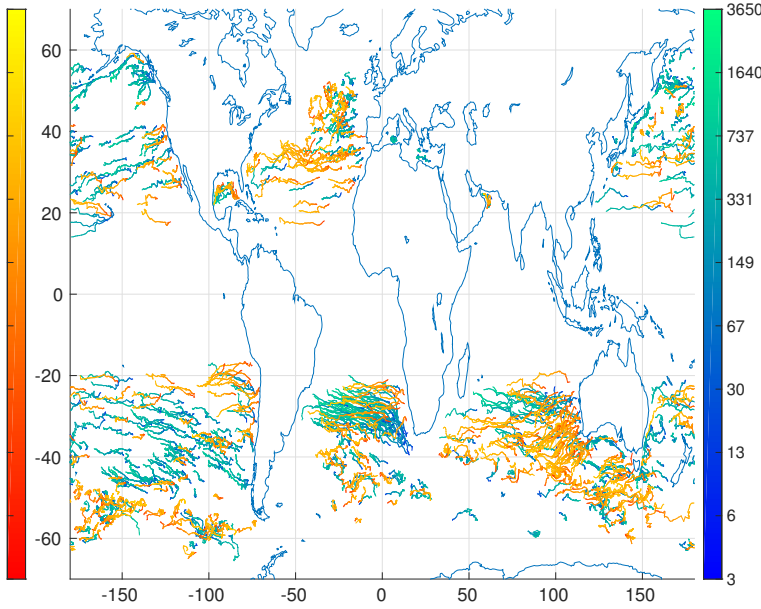


Figure 5.11: MII: (see fig. 5.7)

THE IQ-based method results in approximately the same total amount of tracks as the MI method used in section 5.1 (see figs. 5.8 and 5.12). The difference is that tracks here are generally much shorter, meaning that less eddies are detected at any given point in time. The scale  $\sigma$  is now smaller than that from Chelton *et al.* (2011) for all latitudes in zonal-mean as well as median. Westward drift speeds are almost identical to those in section 5.1.

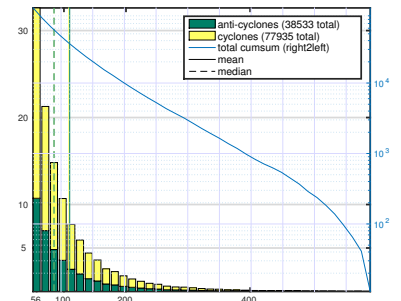
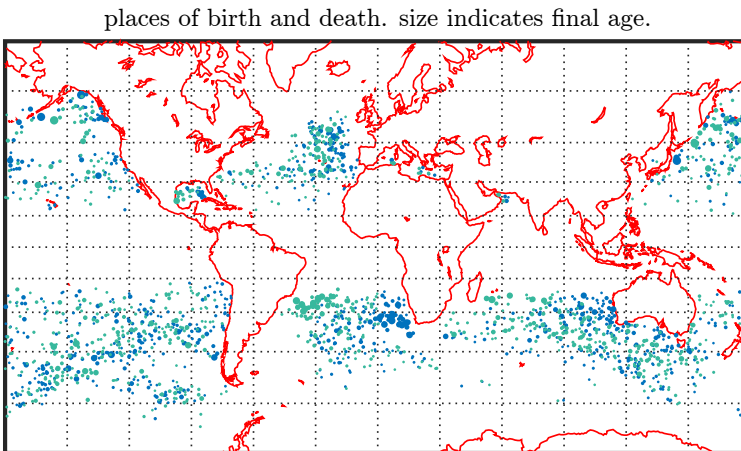


Figure 5.12: Aviso -MII: Final age distribution. x-axis: [days], Left y-axis: [1000].

Figure 5.13: Aviso -MII: Births are in blue and deaths in green. Size of dots scales to age squared. Only showing tracks older than one year.

### 5.3 MII - 7 day time-step - POP

THE model data delivers slightly more total tracks with a similar 2-fold dominance of cyclones over anti-cyclones (compare figs. 5.12 and 5.14). Similar to Aviso-MII , very long tracks are fewer than via Aviso-MI <sup>4</sup>. The regional pattern looks somewhat similar to the satellite patterns in terms of which regions feature the strongest eddy activity. With the exception of an unrealistic abundance of eddies right along the Antarctic coast where no eddies were detected for the satellite data, likely due to sea ice and/or the inherent lack of polar data due to the satellites' orbit-inclinations.

THE more important difference between model- and satellite regional distributions is that the model results indicate significantly less eddy activity away from regions of strong SSH gradients, in the open ocean away from coasts and strong currents. The algorithm also detects hardly any eddy tracks in tropical regions (see fig. 5.4). This regional heterogeneity in eddy-activity in the model data is also reflected in the distribution of eddy amplitudes (see fig. A.2).

THE scale  $\sigma$  is generally smaller for the model-data-based analysis than for any satellite-based analyses, especially so in high latitudes.

WESTWARD DRIFT SPEEDS look regionally similar to those from satellite data (figs. 5.6 and 5.16). In the zonal mean their magnitude is below those from satellite (see fig. 5.17).

<sup>4</sup> Aviso-MI features 3000 tracks that are older than 400 days, while both MII methods have only  $\sim 1000$  of such.

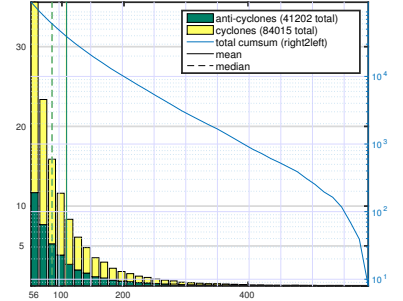


Figure 5.14: pop7-MII: Final age distribution. x-axis: [days], Left y-axis: [1000].

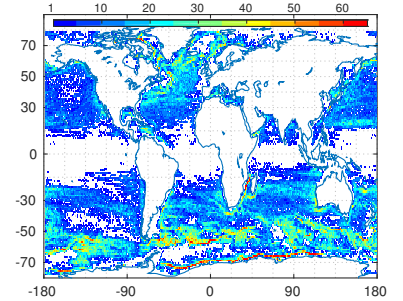


Figure 5.15: pop7-MII: Total count of individual eddies per 1 degree square.

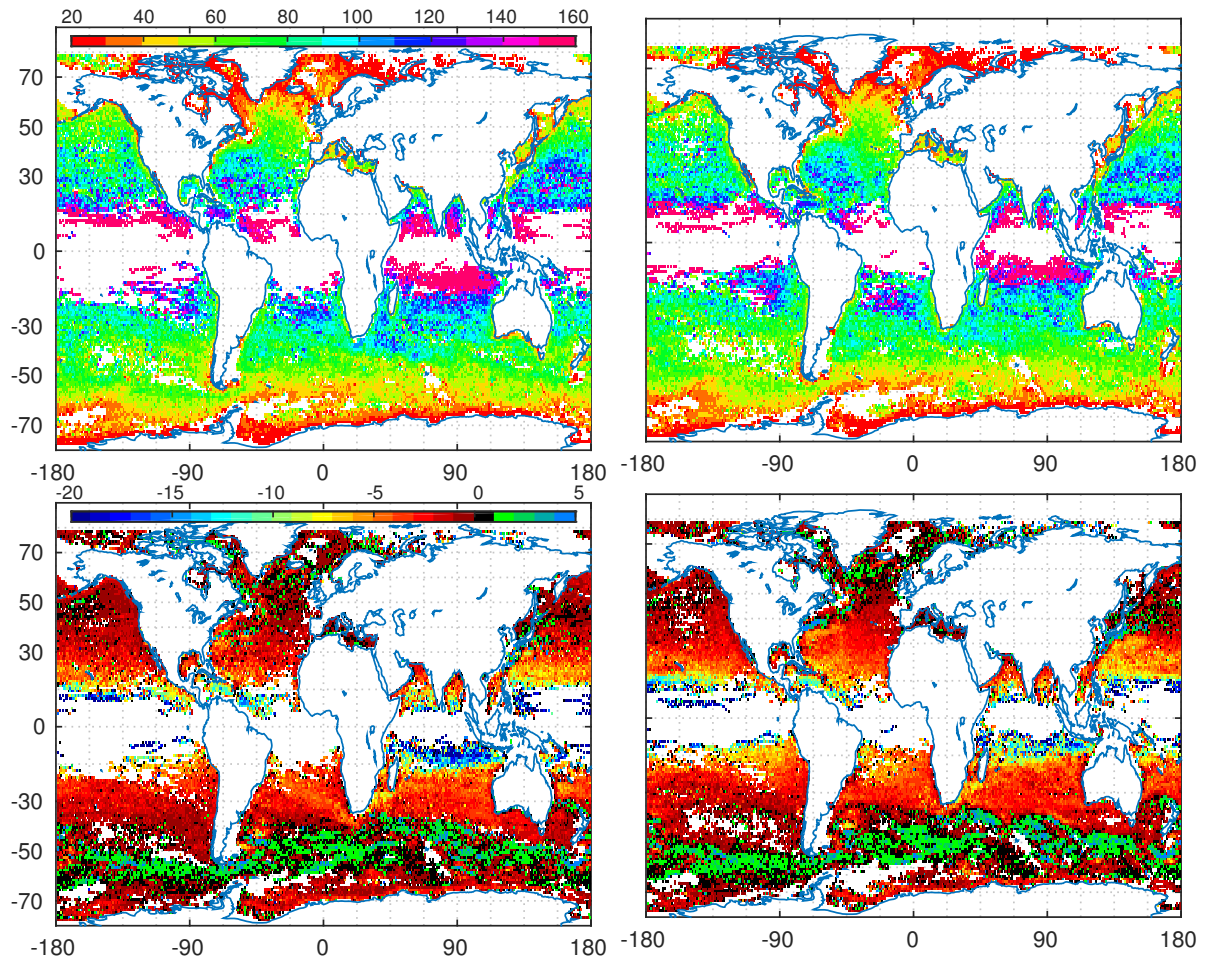


Figure 5.16: pop7-MII: . Top:  $\sigma$  [km].  
Left: Anticyclones. Right: Cyclones. Bottom: zonal drift speed [cm/s]. Left: Anticyclones. Right: Cyclones.

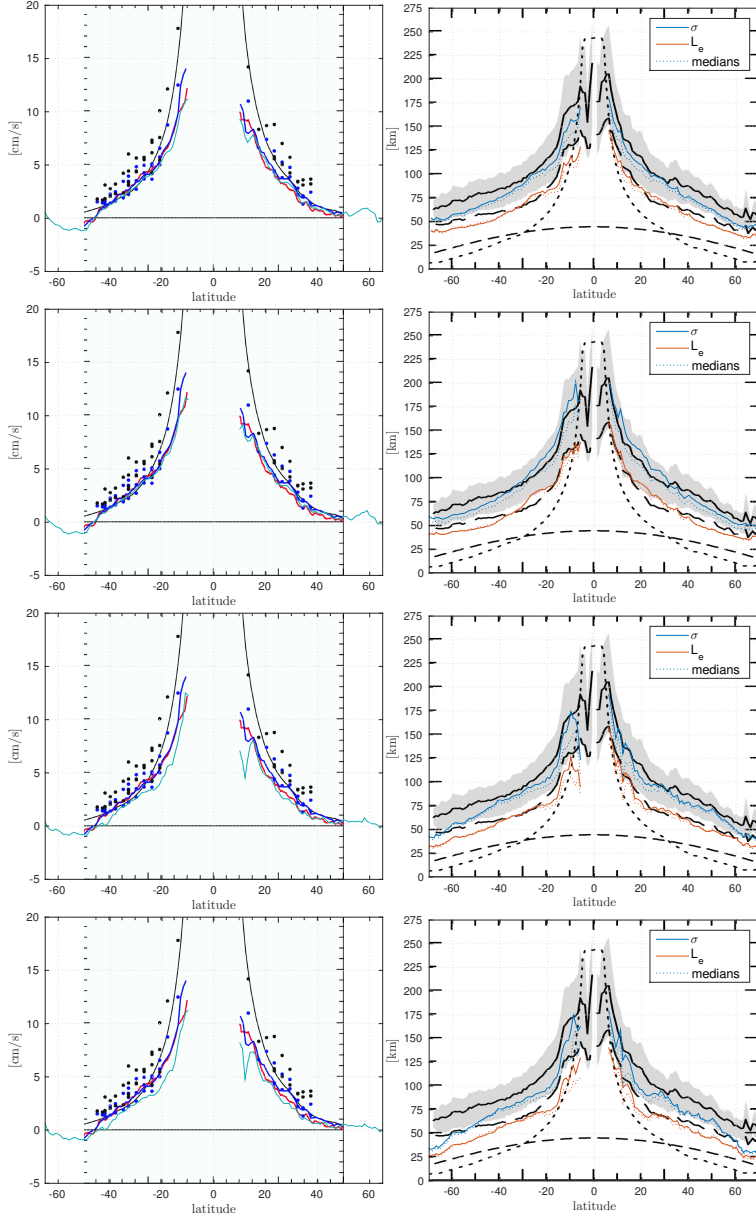


Figure 5.17: Left: Zonal-mean drift speed (cyan) fit to Fig 22 of (Chelton *et al.*, 2011) (Background). Right:  $\sigma$  and  $L_e$  fit to Fig. 12 of their paper. Dotted lines are medians instead of means. 1st row: Aviso-MII , 2nd row: Aviso-MI , 3rd row: pop2avi-MII , 4th row: POP-7day-MII . Note that for the very high latitudes ( $> |60^\circ|$ ) the contrast between model and satellite data is further intensified by the lack of satellite data (see fig. 5.5) in those regions (sea-ice / orbit inclinations). For a depiction without this effect see fig. 6.4. Regarding the underlying figures Chelton *et al.* explain: [Left] The black dots are the Radon transforms of the  $20^\circ \times 10^\circ$  high-pass filtered SSH fields along [...] zonal sections [...] The red dots are the average along the propagation speeds of eddies with lifetimes  $> 16$  weeks within  $\pm 1.5^\circ$  of latitude of the center latitudes of the same 45 zonal sections. The latitudinal profile of the global zonal average of the propagation speeds of all of the eddies with lifetimes  $> 16$  weeks is shown by the red line [...]. The black line is the latitudinal profile of the zonally averaged westward phase speeds of long baroclinic Rossby waves. [Right] [...] Meridional profiles of the average (solid line) and the interquartile range of the distribution of  $L_s$  (gray shading) in  $1^\circ$  latitude bins. The long dashed line is the meridional profile of the average of the e-folding scale  $L_e$  of a Gaussian approximation of each eddy [...]. The short dashed line represents the  $0.4^\circ$  feature resolution limitation of the SSH fields of the AVISO Reference Series for the zonal direction [...] and the dotted line is the meridional profile of the average Rossby radius of deformation [...].



# 6

## Discussion

### 6.1 Lengths of Tracks

THE most apparent difference between the results of the [two detection-methods](#) is the abundance of long-lived eddies resulting from the **MI**-method. This discrepancy must logically be caused by the two different contour-shape testing procedures (see [box 3](#) and [contour-filter 8](#)), since it is here where the main difference between the two methods' algorithms lies.

THE **MI**-method is the more lenient one, as all it checks for is whether the contour is of sufficiently compact form. The only shapes that are dismissed are long, thin elongated structures. This means that *e.g.* an eddy track can more easily<sup>1</sup> survive situations in which two eddies merge into one or those in which one is split into two or situations in which mean current gradients distort the vortex (see [fig. 6.2](#)). There could also be the situation in which an old, weak eddy fades, yet another one emerges in sufficient proximity. These two events would not even have to coincide at the exact same time, as long as some short-lived coherent structure, of which there is an abundance<sup>2</sup> at any given time-step throughout the world ocean, acted as a bridge to fill the gap.

<sup>1</sup> as long as the similarity-criterion is not violated.

<sup>2</sup> see [fig. 4.7](#)

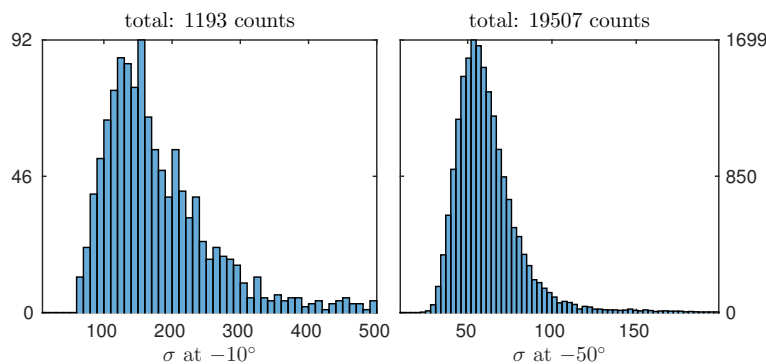


Figure 6.1: **Aviso-MI**  $\sigma$  [km]. Left: Anti-cyclones. Right: Cyclones. Histograms of  $\sigma$  at a low and a high latitude.

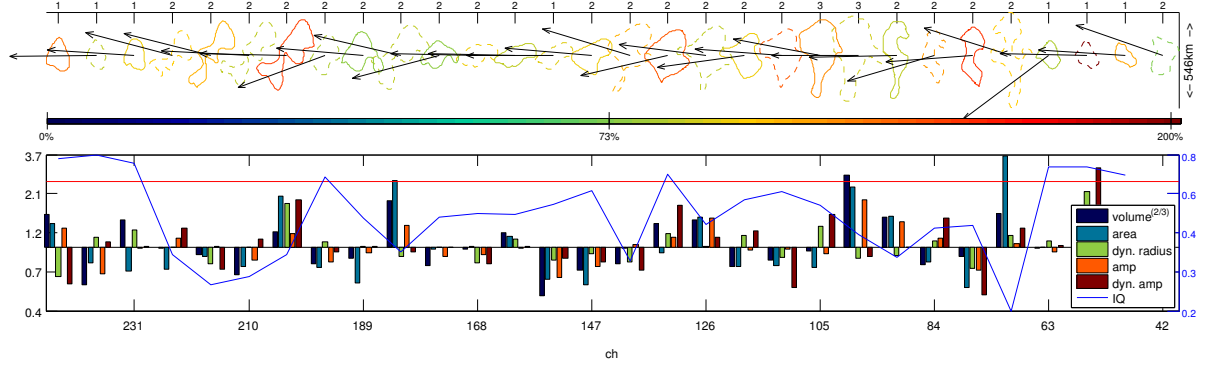


Figure 6.2: The MI-method. Top: Consecutive contours of one track. Colors indicate percentage of change of contour's area with respect to the prior time-step. Topmost horizontal axis shows the (rounded) factor of  $\sigma$  with respect to the local first baroclinic  $L_R^1$ . Vectors' lengths are proportional to the distance traveled with respect to the next time-step. Bottom: Blue graph shows the current IQ. Bars show the factors of change of respective parameters with respect to the prior time-step. X-axis are days since birth.

THE MII-method is conceptually different in that it is based on the assumption that a distinct coherent vortex need *per definition* to be more or less circular. It will therefore be more likely to regard e.g. the situation in which one eddy merges with another as a situation of 3 eddies in total; **two** that have just died to create **one** new one. The focus here is more on the propagation of distinct circular geostrophic vortices whereas the focus in the MI-method is more general on coherent local depressions respective elevations in SSH (see fig. 6.3). It should be interesting to look at to which degree tracers found within tracked eddies remain within the eddy over time (postponed for now). This could further clarify the hypothesis that the MI-method might be better at tracking water-mass advecting entities, with less jumps between bodies of water within one track. E.g. looking at temperature/salt at the eddy's core as a function of time. The downside of the IQ-method is that the identity checks between time-steps fail more easily in the case of merging/splitting situations, thus cutting tracks short. I.e. in the case of one large eddy absorbing another, it does not *die*, but its contour becomes temporarily disfigured and it might thus fail the id check. It comes again down to a question of definition *i.e.* if one large eddy splits into two small ones are we talking about three, or two unique eddies in total?

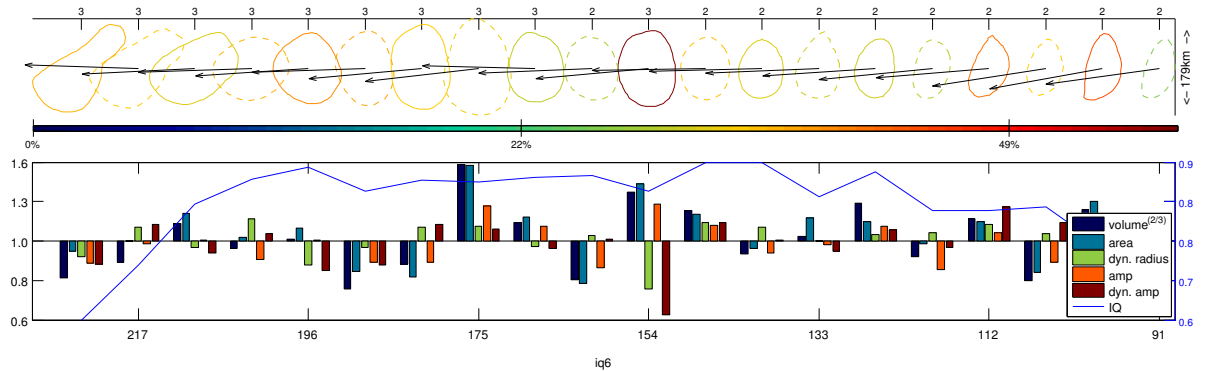


Figure 6.3: The MII-method (IQ threshold at 0.6) (see fig. 6.2).

## 6.2 Scales and the Effect of Down-Sampling

INTERESTINGLY, even in the **Aviso-MI** results, the horizontal eddy scale  $\sigma$  differs from that presented by **Chelton et al.** (2011). For latitudes  $\gtrsim |25^\circ|$  the zonal mean here is smaller than theirs while for low latitudes it is higher (see figs. 5.17 and 6.4). The reason for this discrepancy is suspected to stem from the special method by which  $\sigma$  is determined by our algorithm. As outlined in contour-filter 12, here  $\sigma$  is half the mean of zonal and meridional distances between the first two local extrema of the first derivative of interpolated 4th-order Fourier fits to the **SSH** data around the eddy's CoV. **Chelton et al.** calculate the respective scale via *a direct estimate based on the contour of **SSH** within the eddy interior around which the average geostrophic speed is maximum*. I.e. they derive  $\sigma$  directly via the area described by the contour of maximum  $|\nabla u|$  and not via any Fourier-type fit.

THE motivation to use fits instead of the **SSH** directly was on the one hand to avoid noise complicating correct determinations of the 2nd differential zero-crossings and on the other hand to tackle the problem of coarse resolution, especially so for high latitudes where  $\sigma$  seems to become as small as only twice the distance between data points. At this resolution the Gaussian RMS width of an eddy would amount to only 5 data points. Since  $\sigma$  is generally smaller in the higher-resolution **POP**-data analyses, we hypothesize that the scales by **Chelton et al.** are biased high for high latitudes. Question remains to what degree this bias is inherent to the **Aviso** product *i.e.* as a smearing effect from the interpolation of multiple coarse satellite data. Or whether it is attributable entirely to the particular method by which the diameter/area of the zero-vorticity contour is estimated.

WITH REGARD to the lower latitudes two important aspects need to be considered:

1. The analyses yield generally low eddy activity in the tropics. Hence the results are less robust in this region *a priori*.
2. The standard deviation in  $\sigma$  is particularly broad in the tropics (see fig. 6.5). As a matter of fact it appears as though there might be two different types of eddies. One type analogous to all high-latitude eddies and a new one of much larger scale. Because these larger eddies have generally low IQ-values, they are filtered from the **MII** analyses, resulting in smaller tropical  $\sigma$ . Their more chaotic shape might, due to the different methods to determine  $\sigma$ , also have to do with

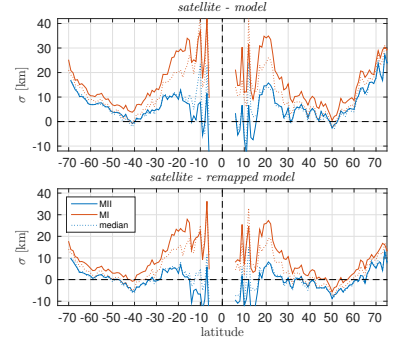


Figure 6.4: Differences in zonal mean  $\sigma$  between **Aviso/POP** and **Aviso**/down-sampled **POP**. Means/medians are built zonally over only those  $1^\circ \times 1^\circ$ -bins that feature data in both sets *i.e.* the intersection of  $lat + 1i \ lon$  of both sets.

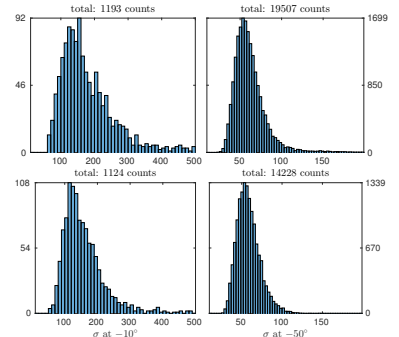


Figure 6.5: Eddy count at one point in time for one fully zonal  $1^\circ$ -bin. Top: **Aviso-MI**. Bottom: **Aviso-MII**. The tropical spectrum is broad yet with strong positive skewness *i.e.* oriented towards smaller scales. In high latitudes the standard deviation is smaller. The **MI** method yields more large eddies.

why mean tropical  $\sigma$  is larger here than in [Chelton et al. \(2011\)](#).

THE **POP-7day-MII** analysis yields somewhat similar  $\sigma$  for low latitudes<sup>3</sup>, yet significantly smaller values for high latitudes. The question here therefor is whether this discrepancy is a result of the lower resolution of the satellite data *i.e.* that eddies are too small to be resolved by the [Aviso](#) product in high latitudes or whether it is attributable to the model data as in a systematic bias due to incomplete/poorly parameterized model physics. This question was the primary motivation for the **pop2avi-MII**-run. The idea here was to down-size the **POP** data to the geometry of the [Aviso](#) grid in order to test whether this would raise  $\sigma$  to that from the satellite results. Figure 6.4 shows that the down-sampling did indeed decrease the discrepancy in  $\sigma$  to that of the respective [Aviso](#) analysis, as long as those regions that are unique to either data set are excluded. Between  $\pm 25^\circ$  and  $\pm 65^\circ$  the difference is no larger than  $\pm 5$  km. This came as a surprise because since  $\sigma$  stems from Fourier fits of SSH, we expected the original frequencies to be, at least to some extent, conserved in the coarsened resolution (see also fig. 6.6). Nevertheless, scales away from the tropics are much larger still than the **linear** local first-mode baroclinic Rossby radius. The reason for this likely has to with the fact that, away from the tropics, linear theory becomes an increasingly poor description of turbulent geostrophic dynamics.

### 6.3 Drift Speeds

ZONAL mean drift speeds of all [Aviso](#) results agree well with those presented by [Chelton et al. \(2011\)](#) (see fig. 5.17), suggesting that the tracking procedures are relatively robust for both the **MI** and **MII** methods.

THE **POP-7day-MII** results yield generally smaller magnitudes of drift speed. The apparent drop at  $\approx 12^\circ\text{N}$  is most likely due to erroneous inter-time-step eddy-associations (fig. 5.17). In that region, the combination of extreme sparsity of results, large time-step, large  $\sigma$ , low amplitude and high (theoretical) drift speed make robust determinations of  $u$  practically impossible. Yet the tendency for lower magnitudes in  $u$ , albeit less stark, is also true for higher latitudes. The zonal drift speeds are calculated via gradients of *poly-fits* to the **CoV**-locations on the surface of a spherical earth. This method was tested thoroughly and its robustness is further validated by the fact

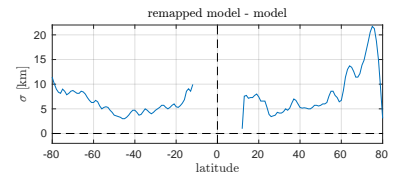


Figure 6.6: Difference in  $\sigma$  between **pop2avi-MII** and **POP-7day-MII**.

<sup>3</sup> Note that due to the lack of tropical eddies the estimates of  $\sigma$  are rather uncertain for the **POP** analyses.

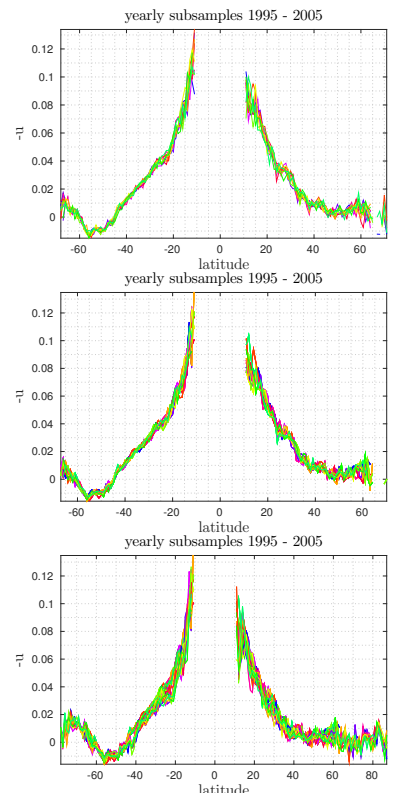


Figure 6.7: Each of the 11 lines represents zonal means of tracks that ended within one of the eleven years from 1995 to 2005. Top: [Aviso-MI](#). Middle: [Aviso-MII](#). Bottom: [POP-7day-MII](#).

that the weaker  $u$  remains approximately the same after down-sampling for the `pop2avi-MII` run. Yearly sub-samples of the zonal-mean profiles (section 6.3) further prove the consistency of the drift-speeds over time for both data.

FROM equation (3.1) we know that at first approximation (planetary lift)

$$u \sim \beta \left( \frac{NH}{f} \right)^2 \quad (6.1)$$

Since  $\beta, H$  and  $f$  should have been set realistically in POP, it appears that the, evidently unrealistic, drift speeds in the model results stem from an unrealistic or poorly resolved (only 42 vertical layers in POP) density stratification  $\frac{\partial \rho}{\partial z}$ .

STRONG zonal skewness with opposite sign of  $u$  in all analyses (see fig. 6.9) suggests the existence of many values much smaller in magnitude than the median that smear the distribution of drift speeds towards an unrealistically low mean. This effect appears to be relevant in e.g. the Southern Ocean, where the east-ward advection of eddies by the ACC results in a broad spectrum of drift speeds. The strong gradients in mean current also effect an abundance of eddy -merging and -splitting situations over relatively short periods of time. It is therefore difficult for the algorithm to keep track of sufficiently long-lived, coherent vortices. Especially so for large time-steps and a high age-threshold. Yet, if the minimum time-step is limited, as in the case of satellite data, a high age-threshold is necessary since short tracks with few data points in time are more likely to stem from erroneously matched contours that do not represent the actual track of a single vortex but instead represent other mesoscale noise that happened to feature sufficiently similar blobs popping in and out of existence at sufficient proximity to one another.

A general problem with the depiction of drift-speeds as zonal means is that  $u$ , besides latitude, is also strongly dependent on longitude. Figures 5.10 and 5.15 show strong regional heterogeneity of  $u$  presumably influenced by  $f/H$ -contours, density stratification and mean flow (Petersen *et al.*, 2013; Olbers *et al.*, 2012). Note, for example, how the area at 15°S west of Australia shows regional drift speeds of  $u = < -15 \text{ cm/s}$  whilst the zonal mean of  $u$  amounts to only  $\approx -6 \text{ cm/s}$ . It appears that generally areas of strong eddy activity yield larger values for  $u$  than do areas of weaker mesoscale dynamics (see also figs. 4.2, 6.9 and A.2).

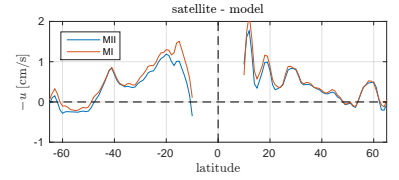


Figure 6.8: Aviso-MI / Aviso-MII minus POP-7day-MII of zonal drift speed means.

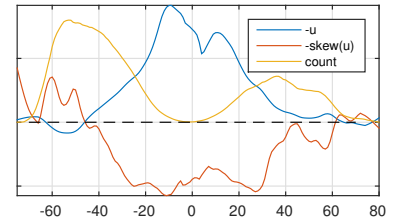


Figure 6.9: Skewness (red) of  $-u$  for Aviso-MI. The spectrum leans towards high westward values in low latitudes. In the ACC the distribution reverses, indicating a bulk eastward advection by the mean flow combined with more sporadic (in time or space (x-dir.)) events of slower (eastward) and also westward propagation (which of course stems from the meridional heterogeneity of the ACC current vectors). Note: Everything normalized to fit all in one frame.

#### 6.4 MII - 2 day time-step - POP

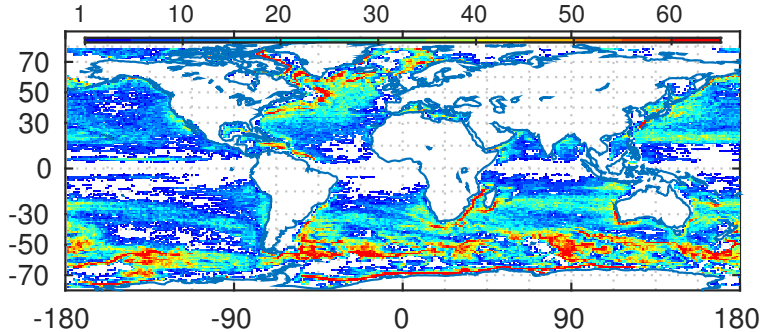


Figure 6.10: POP-2day-MII : Count per  $1^\circ \times 1^\circ$  box of individual eddies. The finer time step results in a higher total count of unique eddies.

So far, all analyses used a 7 day-time-step. As already mentioned in section 2.4, from the results we know that eddies translate at speeds on the order  $\mathcal{O}(10^0) \text{ cm s}^{-1}$  to  $\mathcal{O}(10^1) \text{ cm s}^{-1}$  or up to  $100 \text{ km/7 day}$  and apparently even more in low latitudes. This means that one eddy's location might well change as much as its own scale and more over one time-step. Considering how tightly packed eddies often are in areas of high activity, *i.e.* directly adjacent to one another akin to an egg's box (see *e.g.* fig. 4.7), raises the issue whether the weekly resolution in time is sufficient to successfully track individual eddies and thus deliver realistic translative-speed statistics. In order to investigate the influence of a shorter time-step, the POP-7day-MII run was repeated, only this time with a 2 day time-step.

The effect is only small in the zonal mean (see fig. 6.11). But regionally some noteworthy differences to the weekly frame rate emerge (see fig. 6.12):

- Westward drifts are now faster in low latitudes, suggesting that the 7-day time-step is indeed too large to correctly associate all of the large, fast tropical eddies.
- Areas of strong drift-speed gradients as along the western boundary currents and the ACC show slight general disagreement between the two analyses, suggesting that the analysis benefits from more available time-frames.

#### 6.5 Net Drift Speeds

The reversal in drift direction within all sufficiently strong eastward currents (*e.g.* ACC) shows that the, naturally westward-propagating, eddies get advected by mean flows, analogous to eastward-moving pressure systems spawned off of the atmospheric jet-stream. Since 3-dimensional current-vectors

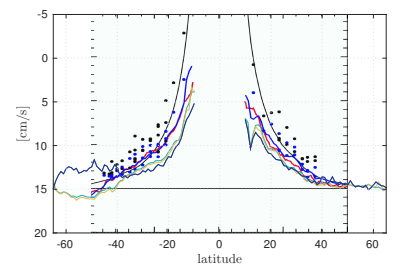


Figure 6.11: Same plot as the POP-7day-MII one from fig. 5.17 with the result from POP-2day-MII appended in ocher. Dark blue shows POP-2day-MII result with vertically averaged (surface to 2000 m) mean current subtracted (see section 6.5).

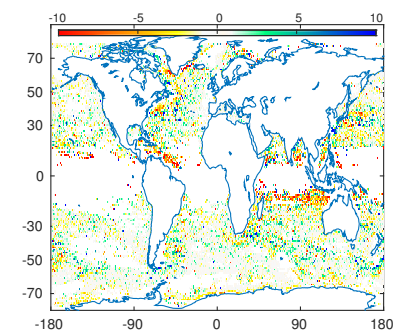
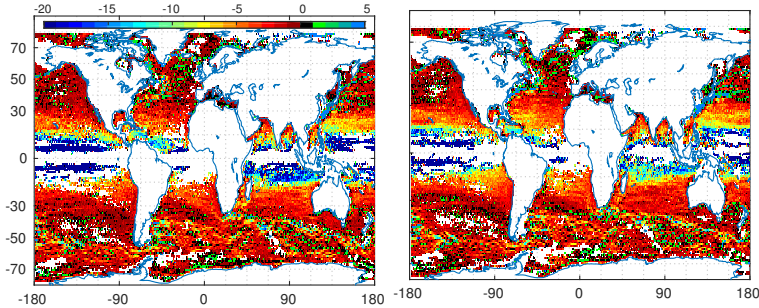


Figure 6.12: Zonal drift speed of POP-2day-MII minus POP-7day-MII [ $\text{cm s}^{-1}$ ].

are available for the model-data, it should be possible to subtract this *Doppler-shift*, in order to extract maps of theoretical drift-speeds without advection by mean-currents. For this to be successful, information about the vertical extent of eddies *i.e.* their thickness is indispensable since horizontal current speeds usually have a significant vertical dependence. The vertical structure of eddies is beyond the scope of this work<sup>4</sup>. Therefor it was decided to simply average the horizontal background current (time-mean over 2 years) vertically from surface to some depth  $z_{cb}$ . From the thickness maps of Petersen *et al.* (2013), it appears that there are regions with eddy thickness' of  $z_{cb} \approx 1000$  m and regions with  $z_{cb} \approx 2000$  m. Subtracting the constructed background current mean at  $z_{cb}$  set to 2000 m from the eddy drift speeds has first and foremost the effect that the net eastward translation of eddies throughout the ACC disappears (see fig. 6.13). This suggests that the tall ACC eddies are indeed simply advected by the deep-reaching background current. The mechanism by which the eddies propagate west (see drift-speed-box 2.2.2) applies relative to the medium it is surrounded by. Both, the planetary-lift- and the  $\beta$ -internal-effect are independent of the translation vector of the eddy itself.



<sup>4</sup> For a discussion of preliminary experiments regarding the vertical structure see appendix A.

Figure 6.13: Zonal drift speed of POP-2day-MII minus vertical mean from 1m to 2000m of mean background current [ $\text{cm s}^{-1}$ ].





The results of this thesis can be summarized as follows:

1. Away from the tropics, the meridional profile of the speed-based scale, that is the radius from the eddy's center to the contour of fastest particle orbit, appears to grow linearly with latitude and is several times larger than the local first-mode baroclinic Rossby radius. In the tropics, results are sparse and less robust, but aforementioned eddy scale and Rossby radius seem to agree better here. Implementing a stricter shape constraint results in a smaller horizontal scale and intensifies the contrast in scale between tropics and higher latitudes.
2. By comparing determined zonal drift speeds from an analysis with a 7-day time-step to those from a 2-day time-step, we show that the success rate of automated tracking of individual eddies, albeit satisfactory for most parts of the world ocean, decreases considerably in regions of strong background-current gradients at the weekly time-step. This decreases the quality of determined drift speeds, drift trajectories and eddy life-spans locally. Zonal drift speeds agree well with first-order long baroclinic Rossby wave phase speeds, except for those regions where strong background currents advect the eddies.
3. The POP census yields generally smaller horizontal scales (albeit still much larger than  $L_R^1$ ), especially in high latitudes. This discrepancy is mitigated by interpolating the POP SSH grids to the geometry of the Aviso product, suggesting that the primary reason for the discrepancy is the coarse resolution of the Aviso-product.

Zonal drift speeds derived from the model data are smaller in magnitude for all latitudes than those stemming from the satellite data. Since determined drift speeds are generally robust and constant among yearly sub-samples, the discrepancy is speculated to stem from imperfect model physics as e.g. poor vertical resolution of density.

Sea-surface-signature-based interpretation of geostrophic mesoscale ocean dynamics via space-born altimeter products has come a long way since the launch of the [Topex/Poseidon](#) mission. In the early years, few years of data and poor spatial resolution led oceanographers to still construe the westward drifting pattern of [SSH](#) anomalies as Rossby waves ([Le Traon & Minster, 1993](#); [Killworth et al., 1997](#)). Merging the [Topex/Poseidon](#) with the [ERS-1/2](#) altimeter output increased the resolution by a factor of 2 ([Chelton et al., 2007](#)), revealing that most of the [SSH](#) variability had in fact to be accredited to non-linear mesoscale eddies. Today, the availability of a long, coherent time-span of weekly, spatially consistent [SSH](#) data, makes global automated eddy-identification and -tracking feasible. When interpreting censuses as such, consideration of the technical methods and thresholds used in the algorithm is important. The spectrum of geostrophic phenomena does not allow for sharp discriminations between the theoretical concepts of Rossby waves, geostrophic currents and coherent vortices. The stringencies of the algorithm in terms of amplitude, shape, size, lifespan etc. effectively **define** the object under investigation. Generalized statements about *eddy* statistics derived from such censuses hence always hinge on the understanding of what an eddy is and how this understanding had been implemented in the algorithm.

# A

## Ideas for the Future

Beyond the topics discussed in this study, further ideas led to several additional, mostly incomplete implementations of tools to further investigate eddy dynamics via automated tracking. The following are a handful of examples of topics to address subsequent to this work.

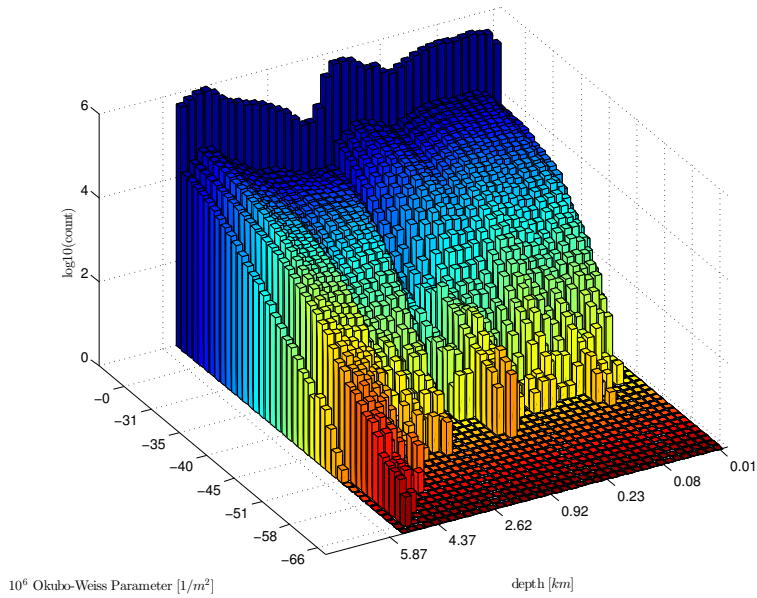


Figure A.1: Histogram of global  $O_w$  as a function of depth calculated from POP current vectors. The idea was to find the surface  $z_{ow}(y, x)$  of maximum  $-O_w(z, y, x)$  and then use that depth as the depth to take the mean current from (see section 6.5). The maximum tends to be at the ocean floor which led to the conjecture that the numerical implementation of  $O_w$  might have been erroneous. Further application was hence abandoned.

- **Applying the algorithm at different depths**

One advantage of using model data is that it is not limited to the sea surface. All parameters are also available for all of the vertical levels. In order to apply the same algorithm that was used for SSH at depth, barotropic pressure plus density integrals were used to construct virtual SSH anomalies for different depths. Preliminary results were promising and seemed to agree well with the findings by Petersen *et al.* (2013) with respect to the regional distribution of eddy-thicknesses. Since the necessary temperature- and salt-data were available for merely 2 years and because computational resources were first and foremost needed for the surface-analyses, this chapter was abandoned entirely for now. The three-dimensional structure should certainly be the focus from here on, as its physics are thus far neither well observed nor understood. Petersen *et al.* e.g. note that even though the majority

of long-lived eddies do extend all the way to the surface, still thousands of tall, sub-surface eddies exist that remain hidden from any sea-surface based detection method. And quoting ([Zhang et al., 2013](#)): *Further study in refining this [vertical] structure is expected, and the refined structure can serve as a benchmark for numerical models where mesoscale eddies are explicitly resolved. In addition, the generation mechanism for this universal structure remains unknown; thus, exploring such mechanism may bring new excitement to eddy research.*

- **Influence of mean flow on drift speeds.**

Knowledge of the vertical scale is also indispensable for investigations of the effect of mean current on eddy dynamics. A considerable amount of time was wasted (to no avail), trying to find vertical local maxima of  $-\Omega_w$  in order to help construct a mean-flow surface taken from respective depths (see fig. [A.1](#)). The idea here was that the depth of strongest  $-\Omega_w$  would be the depth of strongest eddy activity.

Under the assumption that the observed speeds are in fact simply the sum of theoretical long Rossby-wave phase speeds plus the mean flow *i.e.* simple Doppler-shift, another approach would be to look for respective best-fitting depth-range to average the mean-flow over. I.e. seek  $z_1(y, x)$ ,  $z_2(y, x)$  that yield the minimum to

$$c_{rossby,long,x} + \frac{1}{\delta z} \int_{z_1}^{z_2} u_{meanFlow}(z, y, x) dz - u_{observed} \quad (\text{A.1})$$

Where  $z_2$  would likely be the surface.

- **Tracers**

As mentioned in section [6.1](#), it should be interesting to not only track peaks of [SSH](#) anomaly, but parallelly also *e.g.* drop virtual buoys into the centers of eddies and then calculate their positions incrementally from the available current vectors (model only of course). Or simpler, look at basic T/S-watermass characteristics (and their variability) of eddy cores as a function of time. Both could on the one hand illuminate to what degree and under which circumstances the eddy is to be interpreted as a material, watermass transporting vortex as opposed to an immaterial, linear Rossby-wave, and on the other hand help to pin-point mistakes of the tracking algorithm.

- **Track Paths**

Eddy tracks appear to be influenced by bathymetry. Drawing tracks over a map of *e.g.*  $NH/f$  or  $H/f$  contours could further clarify the influence of bathymetry and density gradients on the lateral propagation of eddies.

- **Rhines Scale**

It would be interesting to compare the tropical eddy scales to the local Rhines scale ( $L_\beta$ ) and test whether the theory of the two regimes mentioned by [Eden \(2007a\)](#) can be supported (see also [Tulloch et al. \(2009\)](#)). Eddy identification via [SSH](#) contours is tricky in the tropics where the scales of eddies permit the excitation of linear Rossby waves, resulting in generally less circular structures. Any investigation that focuses on the tropics should hence make use of the [MI](#)-method.

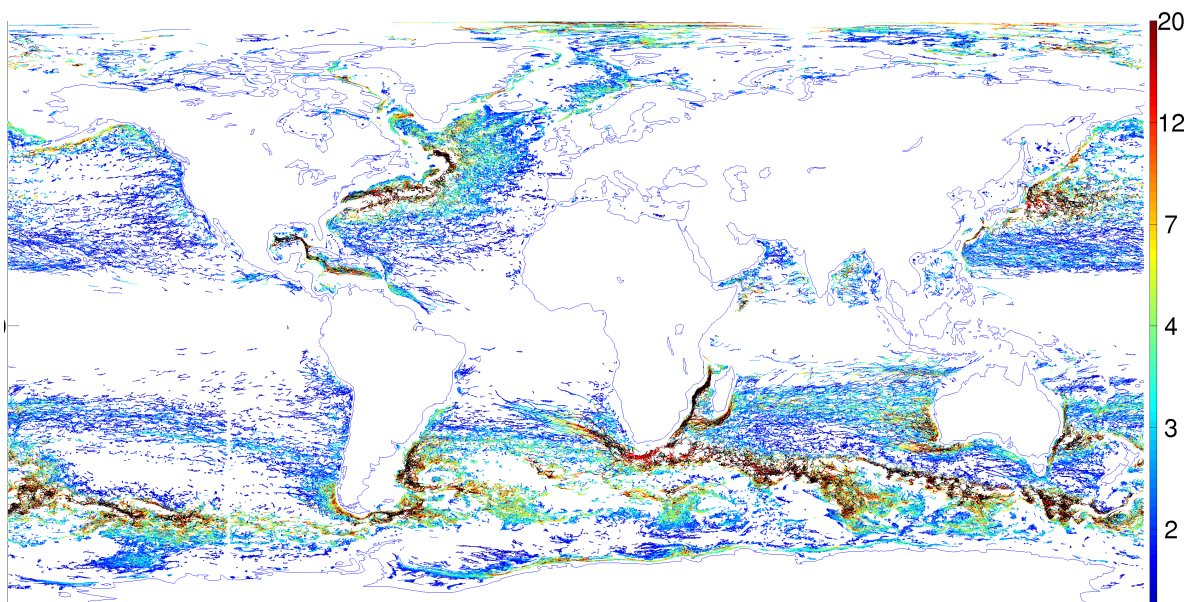


Figure A.2: Amplitude [cm] (w.r. to contour). Tracks are from very early POP test-runs (Note how tracking across the zonal edge of the data was not implemented yet).



## B

### 2-Dimensional Turbulence

THE horizontal scales of planetary geostrophic turbulence are usually so much larger than the vertical, that due to the gyroscopic rigidity of fluid motion in a rotating frame of reference, the turbulence is quasi-invariant in the vertical. Two-dimensional motion has the odd, counter-intuitive quality of cascading towards **larger** instead of **smaller** scales, as would be expected from 3-dimensional flow. This appendix is an attempt to explain this peculiar phenomenon.

$$\frac{Du}{Dt} + \boldsymbol{\Omega} \times \mathbf{u} = -\frac{1}{\rho} \nabla p + \nu \nabla^2 \mathbf{u} + \mathbf{g} \quad (\text{B.1a})$$

$$\frac{Dm}{Dt} = 0 \quad (\text{B.1b})$$

$$\frac{D\omega_a}{Dt} = (\boldsymbol{\omega}_a \cdot \nabla) \mathbf{u} + \mathbf{B} + \nu \nabla^2 \boldsymbol{\omega} \quad (\text{B.1c})$$

$$\frac{DE_k}{Dt} = -\mathbf{u}_h \cdot \frac{1}{\rho} \nabla_h p + \nu \left( \frac{1}{2} \nabla^2 \mathbf{u}^2 - \|\nabla \mathbf{u}\|^2 \right) \quad (\text{B.1d})$$

$$\frac{DE_m}{Dt} = \nu \left( \frac{1}{2} \nabla^2 \mathbf{u}^2 - \|\nabla \mathbf{u}\|^2 \right) \quad (\text{B.1e})$$

$$\frac{D\varepsilon}{Dt} = \boldsymbol{\omega} \cdot (\boldsymbol{\omega}_a \cdot \nabla) \mathbf{u} + \boldsymbol{\omega} \cdot \nu \nabla^2 \boldsymbol{\omega} \quad (\text{B.1f})$$

CONSIDER the equations of motion on a rotating spherical planet with all body forces combined in  $\mathbf{g}$ , which shall always be perpendicular to the surface of a Newtonian fluid at rest. Applying the curl to equation (B.1a) also yields a vorticity equation<sup>1</sup>. Scalar multiplication with  $\mathbf{u}$  reveals a prognostic, kinetic-energy-per-unit-mass budget<sup>2</sup>. Analogously, scalar multiplication of equation (B.2c) with  $\boldsymbol{\omega}_a$  yields an equation for the macroscopic enstrophy density per unit mass<sup>3</sup>. Finally, adding a term for potential energy to equation (B.1d) yields an equation for mechanical energy<sup>4</sup>.

<sup>1</sup> see [derivation 1](#)

<sup>2</sup> see [derivation 3](#)

<sup>3</sup> see [derivation 4](#)

<sup>4</sup> see [derivation 2](#)

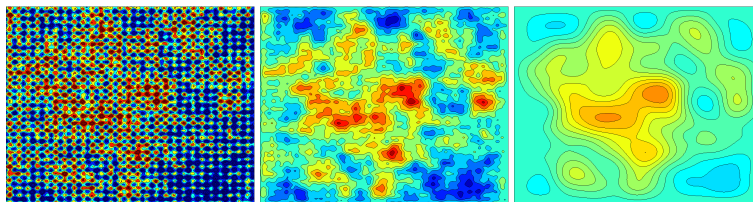


Figure B.1: 1) 2D turbulence with several sinusoidal and random signals as initial condition, 2) at a later time 3) at a much later time. Code from [Seibold \(2008\)](#).

### Turbulence B.1: Non-rotating Tank

CONSIDER first a 3 dimensional non-rotating volume of fluid of constant density with horizontal and vertical dimensions of equal scale. Equations (B.1) then reduce to:

$$\frac{D\mathbf{u}}{Dt} = -\frac{1}{\rho} \nabla p + \nu \nabla^2 \mathbf{u} + \mathbf{g} \quad (\text{B.2a})$$

$$\nabla \cdot \mathbf{u} = 0 \quad (\text{B.2b})$$

$$\frac{D\boldsymbol{\omega}}{Dt} = (\boldsymbol{\omega} \cdot \nabla) \mathbf{u} + \nu \nabla^2 \boldsymbol{\omega} \quad (\text{B.2c})$$

$$\frac{DE_m}{Dt} = \nu \left( \frac{1}{2} \nabla^2 \mathbf{u}^2 - \|\nabla \mathbf{u}\|^2 \right) \quad (\text{B.2e})$$

$$\frac{D\varepsilon}{Dt} = \boldsymbol{\omega} \cdot (\boldsymbol{\omega} \cdot \nabla) \mathbf{u} + \boldsymbol{\omega} \cdot \nu \nabla^2 \boldsymbol{\omega} \quad (\text{B.2f})$$

ASSUMING further the viscosity  $\nu$  of the fluid to be infinitely small, equation (B.2e) and equation (B.2f) reduce to

$$\frac{DE_m}{Dt} = 0 \quad (\text{B.3e})$$

$$\frac{D\varepsilon}{Dt} = \boldsymbol{\omega} \cdot (\boldsymbol{\omega} \cdot \nabla) \mathbf{u} \quad (\text{B.3f})$$

IN the absence of friction, the mechanical Energy of the parcel of fluid is conserved. In contrast, neither enstrophy nor vorticity itself are conserved. Velocity gradients will tilt and stretch the parcel resulting in changes in relative vorticity so as to conserve the parcel's total angular momentum. There is no preference for dimension. The motion is simply turbulent akin to air blowing through a room.

### Turbulence B.2: Rotating Tank

Next consider the tank from turbulence box B.1 to be rotating at some high constant frequency  $\Omega/2 \cdot \hat{z}$ , so that all terms void of  $\Omega$  are small versus those containing  $\Omega$  while all derivatives of  $\Omega$  vanish for its constancy. Again, imagine some magical mix of body forces, so that  $\mathbf{g} \cdot \hat{z} = -g$ .

$$\frac{D\mathbf{u}_h}{Dt} = -\boldsymbol{\Omega} \times \mathbf{u}_h + g \nabla \eta \quad (\text{B.4a})$$

$$\frac{D\boldsymbol{\omega}}{Dt} = \Omega \frac{\partial \mathbf{u}}{\partial z} \quad (\text{B.4c})$$

$$\frac{DE_m}{Dt} = \nu \left( \frac{1}{2} \nabla^2 \mathbf{u}^2 - \|\nabla \mathbf{u}\|^2 \right) \quad (\text{B.4e})$$

$$\frac{D\varepsilon}{Dt} = \boldsymbol{\omega} \cdot \Omega \frac{\partial \mathbf{u}}{\partial z} \quad (\text{B.4f})$$

Equation (B.4a) reveals that in this case all motion must be *quasi* perpendicular to  $\boldsymbol{\Omega}$  and to pressure gradients. Hence  $w \approx 0$  and  $\mathbf{u}_h$  in hydrostatic and geostrophic balance. Equation (B.4c) shows how a stretched or squeezed water column by e.g. a change in water depth results in a dramatic change in relative vorticity. Equation (B.4e) and equation (B.4f) show that again energy is conserved for the  $\text{Re} \gg 1$  case (since our perspective is from the rotating frame of reference, the angular momentum from the rotating tank is a priori irrelevant to  $E_m$ ), and that local enstrophy of a Lagrangian parcel is dramatically changed as soon as the vertical dimension is forced upon the motion.

### Turbulence B.3: Small Aspect Ratio

CONSIDER again the tank, only this time completely flattened, so that its horizontal extent is, say, 3 orders of magnitude larger than its vertical scale. All vertical motion then becomes insignificant and at first approximation the equations reduce to:

$$\frac{\partial \mathbf{u}}{\partial t} + \mathbf{u} \cdot \nabla \mathbf{u} = g \nabla \eta + \nu \nabla^2 \mathbf{u} \quad (\text{B.5a})$$

$$\frac{\partial \omega}{\partial t} + \mathbf{u} \cdot \nabla \omega = \nu \nabla^2 \omega \quad (\text{B.5c})$$

$$\frac{DE_m}{Dt} = \nu \left( \frac{1}{2} \nabla^2 \mathbf{u}^2 - \omega^2 \right) \quad (\text{B.5e})$$

$$\frac{D\varepsilon}{Dt} = \nu \left( \frac{1}{2} \nabla^2 \omega^2 - \|\nabla \omega\|^2 \right) \quad (\text{B.5f})$$

THE main point here is that, for infinitely small viscosity, besides mechanical energy, now also enstrophy is materially conserved. Lacking a third dimension to stretch, squeeze or tilt into, a column of fluid has no mechanism by which to adapt to a change in depth or to a change in ambient vorticity. To investigate this situation further, a scale analysis of the equations of  $E_m$  and  $\varepsilon$  yields:

$$\frac{U^2}{T} + \frac{U^3}{L} = \frac{\nu U^2}{L^2} \quad (\text{B.6e})$$

$$\frac{U^2}{TL^2} + \frac{U^3}{L^3} = \frac{\nu U^2}{L^4} \quad (\text{B.6f})$$

APPARENTLY  $\frac{DE_m}{Dt} \sim L^2 \frac{D\varepsilon}{Dt}$ . Thus, the smaller  $L$ , the more effectively vorticity is advected and burned. Hence enstrophy dominates the turbulence cascade towards smaller scales. Before  $E_m$  gets any chance to cascade itself to ever smaller scales,  $\varepsilon$  is already effectively burning vorticity at large  $k$  and thereby reduces kinetic energy faster than the turbulence cascade can catch up.  $E_m$  being proportional to  $U^2$  cannot compete with  $\varepsilon$  at small scales since  $\varepsilon$  not only scales with  $U^2$  but also with the squared reciprocal of the scale *itself*.

As an analogy I imagine an ice hockey arena being opened instantaneously to 500 people on ice-skates. At first the picture will be highly turbulent with lots of friction among skaters. Sooner or later though, people of like-minded preference for direction and speed are likely to form groups so as to avoid bumping into one another. At some point usually all the people form into one or few large eddies, with those wanting to go faster than others skating at larger radii than the more timid towards the center, whilst those on inadequate orbits get subjected to corrective advection via friction *i.e.* entrainment.

#### Turbulence B.4: $\beta$ -effect

CONSIDER at last the inviscid rotating flat-disk type tank this time in the shape of a shell of a sphere with again  $\mathbf{g} \parallel \hat{\mathbf{z}}$  everywhere perpendicular to the surface at rest. Further assume a strong  $\mathbf{g}$  so that the  $\Omega \cdot \mathbf{y}$  component in the Coriolis term is dwarfed by hydrostaticity. Then with  $f = f\hat{\mathbf{z}} \equiv (\Omega \cdot \hat{\mathbf{z}}) \hat{\mathbf{z}}$  now from a Eulerian perspective:

$$\frac{\partial \mathbf{u}}{\partial t} = -\mathbf{u} \cdot \nabla \mathbf{u} - \mathbf{f} \times \mathbf{u} + g \nabla \eta \quad (\text{B.7a})$$

$$\frac{\partial \boldsymbol{\omega}}{\partial t} = -\mathbf{u}_h \cdot \nabla_h \boldsymbol{\omega} - v \frac{\partial \mathbf{f}}{\partial y} \quad (\text{B.7c})$$

A new term with opposite sign from the  $\boldsymbol{\omega}$ -advection term in  $y$ -direction arises in the vorticity budget, which is evidently most significant where  $f$  changes strongest meridionally, *i.e.* in proximity to the sphere's *equator*. Hence, if scales permit, relative vorticity can now also be altered by a change in latitude via conservation of (total) angular momentum.

# C

## Eddy Categories

Starting from the considerations for equations (B.7) and introducing a variable density, the momentum equations and the z-component of the vorticity equation read:

$$\left(\frac{\partial \mathbf{u}}{\partial t}\right)^i + (\mathbf{u} \cdot \nabla \mathbf{u})^{ii} + (f_0 \times \mathbf{u})^{iii} + (\beta y \times \mathbf{u})^{iv} = (-g \nabla h)^v \quad (\text{C.1a})$$

$$\nabla \cdot \mathbf{u} = 0 \quad (\text{C.1b})$$

$$\left(\frac{D\omega}{Dt}\right)^A + \left(\frac{Df}{Dt}\right)^B = \left(f \frac{\partial w}{\partial z}\right)^C + \left(\omega \frac{\partial w}{\partial z}\right)^D \quad (\text{C.1c})$$

Several balances between terms to maintain vortices are thinkable here:

### Vortex C.1: Frontal Lenses

*large:*  $R_\beta, Bu, U$

*small:*  $Ro, W$

*balance between:*  $ii, iii$  and  $v$

The case with strong density gradients, large current speeds and a Rossby number approaching unity is typical for the meandering tails of turbulent boundary currents and zonal jets as in the Gulf Stream respective cyclogenesis in the atmospheric jet stream. Technically the intra-thermoclinic lenses ([Cushman-Roisin et al., 1990](#)) and strong-density-gradient deep eddies e.g. *meddies* fall into this group as well. With strong stratification, small vertical displacements cause strong pressure gradients. The dynamics can be limited to some thin layer, bottom topography is of little relevance and the surface signal might be small, or misleading.

### Vortex C.2: Small Mid-Latitude Geostrophic Eddies

*large:*  $R_\beta$

*O1:*  $Bu$

*small:*  $Ro$

*balance between:*  $iii$  and  $v$

The true geostrophic eddy with  $L \sim L_R \sim NH/f$ .

**Vortex C.3: Large Geostrophic Gyres**

*small:*  $\text{Ro}, \text{R}_\beta, \text{Bu}$

*balance between:* *iii, iv, v* and friction

The large-scale wind-driven ocean gyres. These can only be interpreted as an *eddy* from the Reynolds-averaged large-scale perspective. The motion is strongly  $f/H$ -contour guided and the  $\beta$ -effect is immediately apparent in their strong western boundary intensification.

**Vortex C.4: the Rossby-wave-eddy**

*large:*  $L$

$\mathcal{O}1:$   $\text{Bu}$

*small:*  $\text{Ro}, \text{R}_\beta$

*balance between:* *iii, iv and v*

In low latitudes quasi-geostrophy and hence a small Rossby number demand large  $L$  and/or small  $U$ . The pressure gradients and hence surface elevation is small. Due to the large meridional extent, slow time-scale and strong  $f(y)$ -gradient, particles moving north or south experience strong changes in planetary vorticity. So much so, that in this regime geostrophic eddies and Rossby waves are no longer clearly separable phenomena.

**Vortex C.5: tornado**

*large:*  $U, g', L_R, \text{Ro}, \text{Bu}, \text{R}_\beta$

*small:*  $L$

*balance between:* *ii and v*

This case is not really applicable to the ocean except for maybe the tropics where  $f$  vanishes (but  $v$  would become relevant) or on small scales in areas of strong tidal currents in combination with bathymetry *i.e. tidal bores etc.* In this case a pressure force would have to be balanced by a centrifugal force alone (*e.g. bathtub*).

*D*  
*Derivations*

### Derivation 1: Vorticity

With the identity

$$\begin{aligned} \mathbf{u} \cdot \nabla \mathbf{u} &= (\nabla \times \mathbf{u}) \times \mathbf{u} + \nabla |\mathbf{u}|^2 / 2 \\ &= \boldsymbol{\omega} \times \mathbf{u} + \nabla \mathbf{u}^2 / 2 \end{aligned} \quad (\text{D.1})$$

equation (B.1a) becomes

$$\begin{aligned} \frac{\partial \mathbf{u}}{\partial t} + \nabla |\mathbf{u}|^2 / 2 + (2\Omega + \boldsymbol{\omega}) \times \mathbf{u} &= -\frac{1}{\rho} \nabla p + v \nabla^2 \mathbf{u} + \mathbf{g} \\ \frac{\partial \mathbf{u}}{\partial t} + \nabla |\mathbf{u}|^2 / 2 + \boldsymbol{\omega}_a \times \mathbf{u} &= -\frac{1}{\rho} \nabla p + v \nabla^2 \mathbf{u} + \mathbf{g} \end{aligned} \quad (\text{D.2})$$

Applying the curl operation to equation (B.1a) and assuming equation (B.1b) for an incompressible fluid yields an equation for the vorticity

$$\begin{aligned} \frac{\partial \boldsymbol{\omega}}{\partial t} + \nabla \times \nabla |\mathbf{u}|^2 / 2 + \nabla \times (\boldsymbol{\omega}_a \times \mathbf{u}) &= \\ = -\frac{1}{\rho} \nabla \times \nabla p - \nabla \rho^{-1} \times \nabla p + v \nabla \times \nabla^2 \mathbf{u} + \nabla \times \mathbf{g} & \end{aligned} \quad (\text{D.3})$$

Annihilating all  $\nabla \times \text{grad}$  and  $\nabla \cdot \nabla \times$  and making use of the identity

$$\nabla \times (\mathbf{A} \times \mathbf{B}) = \mathbf{A} (\nabla \cdot \mathbf{B}) - \mathbf{B} (\nabla \cdot \mathbf{A}) + (\mathbf{B} \cdot \nabla) \mathbf{A} - (\mathbf{A} \cdot \nabla) \mathbf{B} \quad (\text{D.4})$$

equation (D.3) becomes

$$\begin{aligned} \frac{\partial \boldsymbol{\omega}}{\partial t} + \nabla \times (\boldsymbol{\omega}_a \times \mathbf{u}) &= -\frac{\nabla \rho \times \nabla p}{\rho^2} + v \nabla \times \nabla^2 \mathbf{u} \\ \frac{\partial \boldsymbol{\omega}}{\partial t} + (\mathbf{u} \cdot \nabla) \boldsymbol{\omega}_a - \mathbf{u} (\nabla \cdot \boldsymbol{\omega}_a) - (\boldsymbol{\omega}_a \cdot \nabla) \mathbf{u} &= \\ = \mathbf{B} - v \nabla \times (\nabla \times (\nabla \times \mathbf{u})) & \\ \frac{D \boldsymbol{\omega}_a}{Dt} &= (\boldsymbol{\omega}_a \cdot \nabla) \mathbf{u} + \mathbf{B} - v \nabla \times (\nabla \times \boldsymbol{\omega}) \\ &= (\boldsymbol{\omega}_a \cdot \nabla) \mathbf{u} + \mathbf{B} + v \nabla^2 \boldsymbol{\omega} \end{aligned} \quad (\text{D.5})$$

Scaling considerations based on the small aspect ratio e.g. noting that  $\mathbf{B} \sim \nabla p \times \nabla \rho$  is at first approximation limited to the  $x, y$  plane and that  $U/H \gg W/L$  and assuming  $\omega_z \gg \omega_h$ , leads to:

$$\frac{\partial \boldsymbol{\omega}}{\partial t} + \mathbf{u} \cdot \nabla \boldsymbol{\omega} + \beta v \hat{\mathbf{z}} = (\omega_z + f) \frac{\partial \mathbf{u}}{\partial z} + \mathbf{B} \quad (\text{D.6})$$

horizontal:

$$\begin{aligned} \frac{1}{T} \frac{U}{H} + \left( \frac{U}{L} + \frac{W}{H} \right) \frac{U}{H} &\sim \frac{U}{H} \frac{U}{L} + f \frac{U}{H} + \mathbf{B} \\ \Rightarrow \frac{U}{HT} + \frac{U^2}{LH} + \frac{UW}{H^2} &\sim \frac{U^2}{LH} + f \frac{U}{H} + \mathbf{B} \end{aligned} \quad (\text{D.7})$$

vertical:

$$\begin{aligned} \frac{U}{LT} + \frac{U^2}{L^2} + \frac{WU}{HL} + \beta V &\sim \frac{UW}{LH} + f \frac{W}{H} \\ \Rightarrow \frac{U}{LT} + \frac{U^2}{L^2} + \beta V &\sim \frac{WU}{HL} + f \frac{W}{H} \end{aligned} \quad (\text{D.8})$$

Hence at first order:

$$\frac{D \boldsymbol{\omega}_h}{Dt} = (f + \omega_z) \frac{\partial \mathbf{u}_h}{\partial z} + \mathbf{B} \quad (\text{D.9})$$

$$\frac{D \omega_z}{Dt} + \beta v = (f + \omega_z) \frac{\partial w}{\partial z} \quad (\text{D.10})$$

If we further assume quasi-geostrophic motion so that any change in  $\omega_h$  is due to small ageostrophic parallelization of  $\nabla p$  and  $\nabla \rho$  via  $\mathbf{B}$ , the tilting terms vanish, since then  $\boldsymbol{\omega}_h$  is normal to the plane spun by  $\nabla \mathbf{u}_h$  and  $\nabla w$ .

### Derivation 2: Mechanical Energy

Add term for potential energy to equation (B.1d) (assuming  $\nabla \rho = 0$ )

$$\begin{aligned}
\frac{DE_m}{Dt} &= -g\mathbf{u} \cdot \nabla \eta(x, y) + \nu \left( \frac{1}{2} \nabla^2 \mathbf{u}^2 - \|\nabla \mathbf{u}\|^2 \right) + \mathbf{u} \cdot \mathbf{g} \\
\frac{DE_m}{Dt} &= -g\mathbf{u} \cdot \nabla \eta(x, y) + \nu \left( \frac{1}{2} \nabla^2 \mathbf{u}^2 - \|\nabla \mathbf{u}\|^2 \right) - wg \\
&= -g \left( \frac{\partial \eta}{\partial t} + \mathbf{u} \cdot \nabla \eta \right) + \nu \left( \frac{1}{2} \nabla^2 \mathbf{u}^2 - \|\nabla \mathbf{u}\|^2 \right) \\
&= -g \frac{D\eta}{Dt} + \nu \left( \frac{1}{2} \nabla^2 \mathbf{u}^2 - \|\nabla \mathbf{u}\|^2 \right) \\
&= \nu \left( \frac{1}{2} \nabla^2 \mathbf{u}^2 - \|\nabla \mathbf{u}\|^2 \right)
\end{aligned} \tag{D.11}$$

### Derivation 3: Kinetic Energy

Multiply equation (B.1a) by  $\mathbf{u}$ :

$$\begin{aligned}
\mathbf{u} \cdot \left( \frac{\partial \mathbf{u}}{\partial t} + \mathbf{u} \cdot \nabla \mathbf{u} + 2\Omega \times \mathbf{u} \right) &= -\mathbf{u} \cdot \frac{1}{\rho} \nabla p + \mathbf{u} \cdot \nu \nabla^2 \mathbf{u} + \mathbf{u} \cdot \mathbf{g} \\
\frac{1}{2} \frac{\partial \mathbf{u}^2}{\partial t} + \frac{1}{2} \mathbf{u} \cdot \nabla \mathbf{u}^2 + \mathbf{u} \cdot 2\Omega \times \mathbf{u} &= -\mathbf{u} \cdot \frac{1}{\rho} \nabla p + \mathbf{u} \cdot \nu \nabla^2 \mathbf{u} - wg \\
\frac{1}{2} \frac{\partial \mathbf{u}^2}{\partial t} + \frac{1}{2} \mathbf{u} \cdot \nabla \mathbf{u}^2 &= -\mathbf{u}_h \cdot \frac{1}{\rho} \nabla_h p + wg + \mathbf{u} \cdot \nu \nabla^2 \mathbf{u} - wg \\
\frac{1}{2} \frac{\partial \mathbf{u}^2}{\partial t} + \frac{1}{2} \mathbf{u} \cdot \nabla \mathbf{u}^2 &= -\mathbf{u}_h \cdot \frac{1}{\rho} \nabla_h p + \mathbf{u} \cdot \nu \nabla^2 \mathbf{u} \\
\frac{\partial E_k}{\partial t} + \mathbf{u} \cdot \nabla E_k &= -g\mathbf{u}_h \cdot \nabla \eta(x, y) + \nu \left( \frac{1}{2} \nabla^2 \mathbf{u}^2 - \|\nabla \mathbf{u}\|^2 \right)
\end{aligned} \tag{D.12}$$

### Derivation 4: Enstrophy

In 2 dimensions the definition of enstrophy can also be rewritten as:

$$\begin{aligned}
\mathcal{E} &= \int_A \varepsilon \, dA = \int_A \|\nabla \mathbf{u}\|^2 \, dA \\
&= \int_A \left( \frac{\partial v}{\partial x} \right)^2 + \left( \frac{\partial u}{\partial y} \right)^2 + \left( \frac{\partial v}{\partial y} \right)^2 + \left( \frac{\partial u}{\partial x} \right)^2 \, dA \\
&= \int_A \left( \frac{\partial v}{\partial x} \right)^2 + \left( \frac{\partial u}{\partial y} \right)^2 + \left( \frac{\partial v}{\partial y} \right)^2 + \left( \frac{\partial u}{\partial x} \right)^2 - (\nabla \cdot \mathbf{u})^2 \, dA \\
&= \int_A \left( \frac{\partial v}{\partial x} \right)^2 + \left( \frac{\partial u}{\partial y} \right)^2 - 2 \frac{\partial u}{\partial x} \frac{\partial v}{\partial y} \, dA \\
&= \int_A \omega^2 + 2 \frac{\partial u}{\partial y} \frac{\partial v}{\partial x} - 2 \frac{\partial u}{\partial x} \frac{\partial v}{\partial y} \, dA \\
&= \int_A \omega^2 + 2 \frac{\partial u}{\partial y} \frac{\partial v}{\partial x} + 2 \left( \frac{\partial v}{\partial y} \right)^2 \, dA
\end{aligned} \tag{D.13}$$

with  $\nabla \cdot \mathbf{u} = 0$  and appropriate boundary conditions, the last two terms cancel in the integral leaving

$$\mathcal{E} = \int_A \omega^2 \, dA \tag{D.14}$$

### Derivation 5: Okubo-Weiss-Parameter

(using Einstein notation)

$$\begin{aligned}
 O_w &= \text{Tr } \mathbb{T}^2 = \left( \frac{\partial u_i}{\partial x_k} \frac{\partial u_k}{\partial x_j} \hat{e}_i \hat{e}_j \right)_{i,i} \\
 &= \frac{\partial u_i}{\partial x_j} \frac{\partial u_j}{\partial x_i} \\
 &= \left( \frac{\partial u_i}{\partial x_i} \right)^2 + (1 - \delta_{i,j}) \frac{\partial u_j}{\partial x_i} \frac{\partial u_i}{\partial x_j} \\
 &= \left( \frac{\partial u_i}{\partial x_i} \right)^2 + \frac{1}{2} \left( \frac{\partial u_i}{\partial x_j} + \frac{\partial u_j}{\partial x_i} \right)^2 - \frac{1}{2} \left( \frac{\partial u_i}{\partial x_j} - \frac{\partial u_j}{\partial x_i} \right)^2 \\
 &= \frac{1}{2} \left( \frac{\partial u_i}{\partial x_i} + \frac{\partial u_j}{\partial x_j} \right)^2 + \frac{1}{2} \left( \frac{\partial u_i}{\partial x_i} - \frac{\partial u_j}{\partial x_j} \right)^2 + \frac{1}{2} \left( \frac{\partial u_i}{\partial x_j} + \frac{\partial u_j}{\partial x_i} \right)^2 - \frac{1}{2} \left( \frac{\partial u_i}{\partial x_j} - \frac{\partial u_j}{\partial x_i} \right)^2 \\
 &= \text{divergence}^2 + \text{stretch}^2 + \text{shear}^2 - \text{vorticity}^2
 \end{aligned} \tag{D.15}$$

The following interpretation elucidates the relatedness to strain, vorticity and divergence:

$$\begin{aligned}
 O_w &= s_n^2 + s_s^2 - \omega^2 + \nabla \cdot \mathbf{u} \\
 &= (u_x - v_y)^2 + (v_x + u_y)^2 - (v_x - u_y)^2 + (u_x + v_y)^2 \\
 &= (u_x^2 - 2u_x v_y + v_y^2) + (v_x^2 + 2v_x u_y + u_y^2) - (v_x^2 - 2v_x u_y + u_y^2) + 0 \\
 &= (u_x^2 - 2u_x v_y + v_y^2) + 4v_x u_y \\
 &= (u_x^2 + 2u_x^2 + u_x^2) + 4v_x u_y \\
 &= 4u_x^2 + 4v_x u_y
 \end{aligned} \tag{D.16}$$

See also section 2.1.

*E*

## *Legend*

<p><b>Definition 1: Reynolds Number <math>\text{Re}</math> [ ]</b></p> <p>C.compares advection of momentum to frictional acceleration.</p> $\text{Re} = \frac{UL}{\nu}$	<p><b>Definition 8: Steering Level <math>z_S</math> [m]</b></p> <p>The critical depth where the real part of the Doppler shifted phase speed <math>c_1(z_S) = c_1(z) - u(z) = 0</math> vanishes. I.e. the depth where the Doppler shift creates a standing wave, causing the disturbances to grow in place instead of spreading in space, analogous to a <i>supersonic bang</i>.</p>
<p><b>Definition 2: Rossby Number <math>\text{Ro}</math> [ ]</b></p> <p>C.compares advection of momentum to Coriolis acceleration.</p> $\text{Ro} = \frac{U}{fL}$	<p><b>Definition 9: Sea Surface Height <math>\text{SSH}</math> [m]</b></p> <p>Vertical distance to reference geoid. The algorithm uses anomalies with respect to the time-mean.</p>
<p><b>Definition 3: Rhines Number <math>R_\beta</math> [ ]</b></p> <p>Ratio of Rhines scale to horizontal scale.</p> $R_\beta = \frac{U}{\beta L^2} = \frac{a}{L} \text{Ro}$	<p><b>Definition 10: gravitational acceleration <math>g</math> [m/s<sup>2</sup>]</b></p> <p>Value of surface normal component of all body forces.</p>
<p><b>Definition 4: Burger Number <math>\text{Bu}</math> [ ]</b></p> <p>Ratio of relative vorticity to <i>stretching</i> vorticity.</p> $\sqrt{\text{Bu}} = \frac{NH}{fL} = \frac{L_R}{L}$	<p><b>Definition 11: Planetary Vorticity <math>\Omega</math> [1/s]</b></p> <p><math>\Omega = 4\pi/\text{day}_{fix*}</math></p>
<p><b>Definition 5: Isoperimetric Quotient <math>\text{IQ}</math> [ ]</b></p> <p><math>\text{IQ} = A/A_c = \frac{A}{\pi r_c^2} = \frac{4\pi A}{C^2} \leq 1.</math></p> <p>The ratio of a ring's area <math>A</math> to the area <math>A_c</math> of a circle of equal circumference <math>C</math>.</p>	<p><b>Definition 12: Surface-Normal Planetary Vorticity Component <math>f</math> [1/s]</b></p> <p><math>f = f\hat{z} = \Omega \sin \phi \hat{z}</math></p>
<p><b>Definition 6: Rhines Scale <math>L_\beta</math> [m]</b></p> <p>Scale at which earth's sphericity becomes relevant.</p> $L_\beta^2 = \frac{U}{\beta}$	<p><b>Definition 13: Change of Planetary Vorticity with Latitude <math>\beta</math> [m<sup>-1</sup> s<sup>-1</sup>]</b></p> <p><math>\beta = \frac{\partial f}{\partial y} = \Omega/a \cos \phi</math></p>
<p><b>Definition 7: Rossby Radius <math>L_R^x</math> [m]</b></p> <p>The geostrophic wavelength. <math>L_R^x = c_x/f</math></p>	

<b>Definition 14: Okubo-Weiss Parameter</b> $O_w \text{ [s}^{-2}\text{]}$	<b>Definition 23: Layer Thickness/physical height of an isopycnal surface</b> $h(x, y, \rho, t) \text{ [m]}$ $h = H + \eta$ (in the layered model)
Discriminant of characteristic polynomial of deformation tensor. $O_w = \text{strain}_{\text{normal}}^2 + \text{strain}_{\text{shear}}^2 - \omega^2$ A negative value indicates vorticity dominated motion, whereas a positive value indicates deformation. In 2 dimensions with $\nabla \cdot u = 0$ : $O_w = 4(u_x^2 + 4v_x u_y)$	
<b>Definition 15: dynamic eddy scale</b> $\sigma \text{ [m]}$	Average distance from eddy's center to the line of maximum orbital speed <i>i.e.</i> the zero-vorticity contour.
<b>Definition 16: Anti-cyclone (AC)</b>	A vortex with sign of rotational vector opposite to $\Omega$ .
<b>Definition 17: Cyclone (C)</b>	A vortex with sign of rotational vector equal to $\Omega$ .
<b>Definition 18: Rossby-Wave Phase Speed</b> $c_x \text{ [m/s]}$	Global fully non-linear $0^{\circ}6'$ , 1 day, hydrostatic, z-level, Boussinesq, primitive-equation ocean model ( <a href="#">Oestreicher, 2009</a> ). Part of the Community Earth System Model (CESM) ( <a href="#">Maltrud &amp; McClean, 2005</a> ).
<b>Definition 19: Buoyancy Vector</b> $B \text{ [1/s}^2\text{]}$	<b>Definition 26: Aviso - satellite altimetry SSH.</b> Merged ERS-1/2, Topex/Poseidon sea-surface-anomaly product ( <a href="#">Forget, 2010</a> ).
$B = -\frac{\nabla p \times \nabla p}{\rho^2}$	<b>Definition 27: Run Aviso-MI</b> 7-day time-step <a href="#">Aviso</a> with method MI.
<b>Definition 20: Mechanical Energy per mass</b> $E_m \text{ [m}^2/\text{s}^2\text{]}$	<b>Definition 28: Run Aviso-MII</b> 7-day time-step <a href="#">Aviso</a> with method MII.
Sum of kinetic and potential Energy.	<b>Definition 29: Run pop2avi-MII</b> 7-day time-step POP remapped to <a href="#">Aviso</a> -geometry with method MII.
<b>Definition 21: Reduced Gravity</b> $g'(x, y, z) \text{ [m/s}^2\text{]}$	<b>Definition 30: Run POP-7day-MII</b> 7-day time-step POP with method MII.
In the layered model $g' = g \frac{\delta \rho}{\rho_0} = N^2 h$	<b>Definition 31: Run POP-2day-MII</b> 2-day time-step POP with method MII. Minimum Age: 30 day
<b>Definition 22: Brunt Väisälä frequency</b> $N \text{ [1/s]}$	
$N^2 = g / \rho_0 \frac{\partial \rho}{\partial z}$	

*Declaration of Authorship*

I, Nikolaus Koopmann, declare that this thesis titled, *A Global Analysis of Mesoscale Eddy Dynamics via a Surface-Signature-Based Tracking Algorithm* and the work presented in it are my own. I confirm that:

- Where I have consulted the published work of others, this is always clearly attributed.
- Where I have quoted from the work of others, the source is always given. With the exception of such quotations, this thesis is entirely my own work.
- I have not submitted the work to any other examination procedure.
- The submitted printed version is the same as the submitted digital version.

Signed: \_\_\_\_\_

Date: \_\_\_\_\_

*Declaration of Authorship*

Ich, Nikolaus Koopmann, versichere an Eides Statt durch meine Unterschrift, dass ich die vorstehende Arbeit mit dem Titel *A Global Analysis of Mesoscale Eddy Dynamics via a Surface-Signature-Based Tracking Algorithm*, :

- selbständig und ohne fremde Hilfe angefertigt und alle Stellen, die ich wörtlich oder dem Sinne nach aus Veröffentlichungen entnommen habe, als solche kenntlich gemacht habe, mich auch keiner anderen als der angegebenen Literatur oder sonstiger Hilfsmittel - insbesondere keiner im Quellenverzeichnis nicht genannten Internetquellen - bedient habe.
- vorher nicht in einem anderen Prüfungsverfahren eingereicht habe.

Und dass

- die eingereichte schriftliche Fassung der auf dem elektronischen Speichermedium entspricht.

Unterschrift: \_\_\_\_\_

Datum: \_\_\_\_\_



## Bibliography

- Batchelor, George K. 1969. Computation of the Energy Spectrum in Homogeneous Two-Dimensional Turbulence. *Phys. Fluids*, **12**(12), II—233.
- Bjerknes, J., & Holmboe, J. 1944. O the Theory of Cyclones. *J. Atmos. Sci.*
- Brachet, ME. 1988. The dynamics of freely decaying two-dimensional turbulence. *J. Fluid* ....
- Bryan, K, Dukowicz, JK, & Smith, RD. 1999. On the mixing coefficient in the parameterization of bolus velocity. *J. Phys.* ...., 2442–2456.
- Charney, JG. 1971. Geostrophic turbulence. *J. Atmos. Sci.*
- Chelton, Dudley B., Schlax, Michael G., Samelson, Roger M., & de Szoeke, Roland a. 2007. Global observations of large oceanic eddies. *Geophys. Res. Lett.*, **34**(15), L15606.
- Chelton, Dudley B., Schlax, Michael G., & Samelson, Roger M. 2011. Global observations of nonlinear mesoscale eddies. *Prog. Oceanogr.*, **91**(2), 167–216.
- Cipollini, Paolo, Cromwell, David, Jones, Matthew S, Quartly, Graham D, & Challenor, Peter G. 1997. Concurrent altimeter and infrared observations of Rossby wave propagation near 34 N in the Northeast Atlantic. *Geophys. Res. Lett.*, **24**(8), 889–892.
- Cushman-Roisin, Benoit. 2010. *Introduction to Geophysical Fluid Dynamics*.
- Cushman-Roisin, Benoit, Tang, Benyang, & Chassignet, Eric P. 1990. Westward motion of mesoscale eddies. *J. Phys.* ...., **20**(5), 758–768.
- Eden, Carsten. 2007a. Eddy length scales in the North Atlantic Ocean. *J. Geophys. Res.*, **112**(C6), C06004.
- Eden, Carsten. 2007b. Interpreting eddy fluxes. *J. Phys.* ...., 1–34.

- Eden, Carsten. 2012. Implementing diffusivities from linear stability analysis in a three-dimensional general circulation ocean model. *Ocean Model.*, **57**, 15–28.
- Eden, Carsten, & Greatbatch, Richard J. 2008. Towards a mesoscale eddy closure. *Ocean Model.*, **20**(3), 223–239.
- Eden, Carsten, Greatbatch, Richard J., & Willebrand, Jürgen. 2007. A Diagnosis of Thickness Fluxes in an Eddy-Resolving Model. *J. Phys. Oceanogr.*, **37**(3), 727–742.
- Ferrari, Raffaele, & Nikurashin, Maxim. 2010. Suppression of Eddy Diffusivity across Jets in the Southern Ocean. *J. Phys. Oceanogr.*, **40**(7), 1501–1519.
- Flierl, Glenn R. 1984. Rossby wave radiation from a strongly nonlinear warm eddy. *J. Phys. Oceanogr.*, **14**(1), 47–58.
- Forget, Gaël. 2010. Mapping Ocean Observations in a Dynamical Framework: A 2004–06 Ocean Atlas. *J. Phys. Oceanogr.*, **40**(6), 1201–1221.
- Fox-Kemper, Baylor, Ferrari, Raffaele, & Hallberg, Robert. 2008. Parameterization of Mixed Layer Eddies. Part I: Theory and Diagnosis. *J. Phys. Oceanogr.*, **38**(6), 1145–1165.
- Gaspar, Philippe, Grégoris, Y, & Lefevre, JM. 1990. A simple eddy kinetic energy model for simulations of the oceanic vertical mixing. ... *Res. Ocean.* (1978–..., **95**, 179–193.
- Gent, Peter R, Willebrand, Jurgen, McDougall, Trevor J, & McWilliams, James C. 1995. Parameterizing eddy-induced tracer transports in ocean circulation models. *J. Phys. Oceanogr.*, **25**(4), 463–474.
- Goldreich, Peter. 1965. Inclination of satellite orbits about an oblate precessing planet. *Astron. J.*, **70**, 5.
- Griffies, SM. 2004. *Fundamentals of ocean climate models*.
- Isern-Fontanet, J. 2006. Vortices of the Mediterranean Sea: An altimetric perspective. *J. Phys.* ..., 87–103.
- Killworth, PD. 1998. Eddy parameterisation in large scale flow. *Ocean Model. Parameterization*.
- Killworth, Peter D., Chelton, Dudley B., & de Szoeke, Roland A. 1997. The Speed of Observed and Theoretical Long Extratropical Planetary Waves. *J. Phys. Oceanogr.*, **27**(9), 1946–1966.
- Le Traon, P-Y, & Minster, J-F. 1993. Sea level variability and semiannual Rossby waves in the South Atlantic subtropical gyre. *J. Geophys. Res. Ocean.*, **98**(C7), 12315–12326.

- Maltrud, Mathew E., & McClean, Julie L. 2005. An eddy resolving global 1/10 ocean simulation. *Ocean Model.*, **8**(1), 31–54.
- Marshall, David P., & Adcroft, Alistair J. 2010. Parameterization of ocean eddies: Potential vorticity mixing, energetics and Arnold's first stability theorem. *Ocean Model.*, **32**(3-4), 188–204.
- Marshall, JC. 1981. On the parameterization of geostrophic eddies in the ocean. *J. Phys. Oceanogr.*
- Matano, Ricardo P., Schlax, Michael G., & Chelton, Dudley B. 1993. Seasonal variability in the southwestern Atlantic. *J. Geophys. Res. Ocean.*, **98**(C10), 18027–18035.
- Matsuura, Tomonori, & Yamagata, Toshio. 1982. On the evolution of nonlinear planetary eddies larger than the radius of deformation. *J. Phys. Oceanogr.*, **12**(5), 440–456.
- Munk, Walter. 2002. Testimony before the US Commission on Ocean Policy. *Los Angeles, CA*.
- Nof, Doron. 1981. On the  $\beta$ -induced movement of isolated baroclinic eddies. *J. Phys. Oceanogr.*, **11**(12), 1662–1672.
- Oestreicher, Samantha. 2009. Underwater Mathematics : Illuminating Deep-Reaching Ocean Eddies in Climate Models.
- Okubo, Akira. 1970. Horizontal dispersion of floatable particles in the vicinity of velocity singularities such as convergences. *Deep sea Res. Oceanogr. Abstr.*, **17**(143), 445–454.
- Olbers, Dirk, Willebrand, Jürgen, & Eden, Carsten. 2012. *Ocean Dynamics*. Springer.
- Petersen, Mark R., Williams, Sean J., Maltrud, Mathew E., Hecht, Matthew W., & Hamann, Bernd. 2013. A three-dimensional eddy census of a high-resolution global ocean simulation. *J. Geophys. Res. Ocean.*, **118**(4), 1759–1774.
- Rhines, Peter B. 1974. Waves and turbulence on a beta-plane. *J. Fluid Mech.*, **69**(03), 417.
- Rhines, Peter B., & Holland, William R. 1979. A theoretical discussion of eddy-driven mean flows. *Dyn. Atmos. Ocean.*, **3**(2), 289–325.
- Schouten, Mathijs W., de Ruijter, Wilhelmus P.M., van Leeuwen, Peter Jan, & Ridderinkhof, Herman. 2003. Eddies and variability in the Mozambique Channel. *Deep Sea Res. Part II Top. Stud. Oceanogr.*, **50**(12-13), 1987–2003.

- Scott, Robert B, & Wang, Faming. 2005. Direct evidence of an oceanic inverse kinetic energy cascade from satellite altimetry. *J. Phys. Oceanogr.*, **35**(9), 1650–1666.
- Seibold, Benjamin. 2008. A compact and fast Matlab code solving the incompressible Navier-Stokes equations on rectangular domains mit18o86 navierstokes . m Incompressible Navier-Stokes Equations. 1–16.
- Smith, K. Shafer, & Marshall, John. 2009. Evidence for Enhanced Eddy Mixing at Middepth in the Southern Ocean. *J. Phys. Oceanogr.*, **39**(1), 50–69.
- Stammer, Detlef. 1997. Global Characteristics of Ocean Variability Estimated from Regional TOPEX/POSEIDON Altimeter Measurements. *J. Phys. Oceanogr.*, **27**(8), 1743–1769.
- Treguier, AM. 1997. Parameterization of quasigeostrophic eddies in primitive equation ocean models. *J. Phys.* ..., 567–580.
- Tulloch, Ross, Marshall, John, & Smith, K. Shafer. 2009. Interpretation of the propagation of surface altimetric observations in terms of planetary waves and geostrophic turbulence. *J. Geophys. Res.*, **114**(C2), C02005.
- van Leeuwen, Peter Jan. 2007. The Propagation Mechanism of a Vortex on the  $\beta$  Plane. *J. Phys. Oceanogr.*, **37**(9), 2316–2330.
- Weiss, John. 1991. The dynamics of enstrophy transfer in two-dimensional hydrodynamics. *Physica*, **48**, 273–294.
- Zhang, Zhengguang, Zhang, Yu, Wang, Wei, & Huang, Rui Xin. 2013. Universal structure of mesoscale eddies in the ocean. *Geophys. Res. Lett.*, **40**(14), 3677–3681.